ALL-CHALCOGENIDE CORE-SHELL FIBERS FOR NONLINEAR APPLICATIONS

A THESIS SUBMITTED TO
THE GRADUATE SCHOOL OF ENGINEERING AND SCIENCE
OF BILKENT UNIVERSITY
IN PARTIAL FULFILLMENT OF THE REQUIREMENTS FOR
THE DEGREE OF
MASTER OF SCIENCE
IN
MATERIALS SCIENCE AND NANOTECHNOLOGY

By
Bekir Türedi
November, 2015

ALL-CHALCOGENIDE CORE-SHELL FIBERS FOR NONLINEAR APPLICATIONS
By Bekir Türedi
November, 2015

We certify that we have read this thesis and that in our opinion it is fully adequate, in scope and in quality, as a thesis for the degree of Master of Science.

Prof. Dr. Mehmet Bayındır (Advisor)

Assist. Prof. Dr. Bülend Ortaç

Assoc. Prof. Dr. Halime Gül Yağlıoğlu

Approved for the Graduate School of Engineering and Science:

Prof. Dr. Levent Onural
Director of the Graduate School

ABSTRACT

ALL-CHALCOGENIDE CORE-SHELL FIBERS FOR NONLINEAR APPLICATIONS

Bekir Türedi
M.S. in Materials Science and Nanotechnology
Advisor: Prof. Dr. Mehmet Bayındır
November, 2015

The extreme spectral broadening phenomenon called as Supercontinuum generation is considered as one of the most striking phenomenon in nonlinear optics. Due to their broad spectra and uniformly distributed power over the spectra supercontinuum sources have found wide range of applications in areas such as spectroscopy, frequency metrology, optical coherence tomography, microscopy and telecommunications.

In this thesis, we propose a new method to fabricate multicore fibers made of chalcogenide glasses for the use of high power Supercontinuum generation. We designed and fabricated a new seven-core-structured fiber with chalcogenide core /chalcogenide cladding step-index fiber embedded in polymer matrix. After three successful iterative steps we fabricated seven-core chalcogenide glasses fiber which has diameter around 1.35 μm which is engineered to be approximately zero dispersion. The refractive indices of these two materials at 1550 nm are 2.73 and 2.61; as a result the NA is engineered to 0.8 at this wavelength. The step index structure of the fiber provides the very well-confinement of light to the core of the fibers. This enables the more interaction of light with the highly nonlinear part of the fiber and preserves light to be absorbed by the polymer jacket which has high absorbance at IR region. By using split step Fourier method we showed the potential of our fiber to generate supercontinuum covering from 1 μm to 3.5 μm.

Keywords: Nonlinear Fibers, Core-Shell Nanowires, Nonlinear Optics, Supercontinuum Generation, Chalcogenide Glasses, Iterative Size Reduction Method.

ÖZET

LİNEER OLMAYAN UYGULAMALAR İÇİN TAMAMI KALKOJEN ÇEKİRDEK-KABUK FİBERLER

Bekir Türedi
Malzeme Bilimi ve Nanoteknoloji Bölümü, Yüksek Lisans
Tez Danışmanı: Prof. Dr. Mehmet Bayındır
Kasım, 2015

Geniş bantlı ışık üretimi olarak bilinen aşırı spectral genişleme doğrusal olmayan optik alanında en çarpıcı sonuçlardan biri olarak kabul edilir. Geniş spektrumları ve enerjinin spektrum üzerinde düzgün dağılmasından dolayı geniş bantlı ışık kaynakları spektroskopi, frekans ölçümü, optik koherens tomografisi, mikroskopi ve telekomünikasyon gibi değişik alanlarda uygulamaları vardır.

Bu tezde, yüksek güçte geniş bantlı ışık üretimi amacıyla kalkojen camlardan yapılan çok çekirdekli fiberlerin üretilmesi için yeni bir metod sunulmuştur. Bu amaçla polimer matris içine gömülmüş kalkojen çekirdek/kalkojen kılıf kademeli kırıcılık indisine sahip optik fiber dizayn edilip üretilmiştir. Ardarda başarılı üç aşama sonrasında sıfır dağılıma yaklaşık olması için tasarlanmış 1.35 μm toplam çapında yedi çekirdekli kalkojen cam fiberler üretilmiştir. Bu kalkojen malzemelerin kırıcılık indisleri 1550 nm dalgaboyunda 2.73 ve 2.61 olarak ölçülmüştür, bu yüzden numerik açıklığı 0.8 dir. Fiberlerin kademeli kırıcılık indisi yapısı ışığın fiberin çekirdeğinde iyi bir şekilde hapsolmasını sağlamaktadır. Böylece, ışığın fiberin doğrusal olmayan kırıcılık indisi yüksek olan çekirdeğiyle etkileşimi arttırılmaktadır ve ışığın kızıl ötesi emilimi fazla olan polimerle etkileşimi engellenmektedir. Bölünmüş adımlı Fourier methodu (split step Fourier method) kullanılarak üretilen fiberlerin 1 μm'den 3.5 μm'ye kadar geniş bantlı ışık üretebilme potansiyeline sahip olduğu gösterilmiştir.

Anahtar sözcükler: Doğrusal Olmayan Fiberler, Çekirdek-Kabuk Nanokablolar, Doğrusal Olmayan Optik, Geniş Bantlı İşık Üretimi, Kalkojen Camlar, Ardışık Boyut Küçültme Metodu.

Acknowledgement

Firstly, I would like to thank my advisor Prof. Dr. Mehmet Bayındır for providing me a great research environment with a great group.

I am grateful to my research mentor Dr. Tural Khudiyev for being not just a mentor but also a brother for me throughout my master degree.

I am also grateful to laboratory coordinator Murat Dere, and laboratory tecnicians Seyit Ali Yaşar, and Serkan Güler who helped me a lot during my research. They performed their best for me everytime.

I also would like to thank all of the Bayındır Group members: Abubakar Adamu, Dr. Ozan Aktaş, Ahmet Başaran, Pınar Beyazkılıç, Hale Nur Çöloğlu, Bihter Dağlar, Emel Gürbüz, Ersin Hüseyinoğlu, Dr. Mehmet Kanık, Dilara Öksüz, Reha Özalp, Neşe Özgür, Fahri Emre Öztürk, Abba Usman Saleh, Pelin Tören, Urandelger Tuvshindorj, Ahmet Faruk Yavuz, Dr. Adem Yıldırım.

I am thankful to my family for their patience, support and love. They always trust me and feed my energy to finish whatever I start.

The special thanks goes to my dear friends -Hamit Eren, Lütfiye Hallıoğlu, Girayhan Say, Murat Serhatlıoğlu, and Muhammad Yunusa- for their friendship, helps, giving me suggestions and most importantly listen me whenever I need.

Financial support from TUBITAK (The Scientific and Technological Research Council of Turkey) is also gratefully acknowledged.

Contents

1 Introduction **1**

2 Background **4**

2.1 Linear Propagation 4

2.1.1 Dispersion 5

2.2 Nonlinear Propagation 7

2.2.1 Numerical Solutions 9

2.2.2 Split-Step Fourier Method 10

2.2.3 Optical Kerr Effect 11

2.2.4 Self-Phase Modulation 12

2.2.5 Cross Phase Modulation 14

2.2.6 Four Wave Mixing 15

2.2.7 Stimulated Raman Scattering 16

2.3 Supercontinuum Generation 17

2.4 Chalcogenide Glasses 19

3 New Fiber Design for High Supercontinuum Generation Output Power in Mid Infrared 22

3.1 Supercontinuum Generation in Optical Fibers 22

3.1.1 Challenges in Supercontinuum Generation with Optical Fibers 23

3.2 Design of Chalcogenide Core/Chalcogenide Cladding Step-Index Seven-Core fiber 27

3.2.1 Dispersion Calculation 28

3.2.2 Single-Mode Profile 33

3.2.3 Supercontinuum Generation Calculations 34

4 Chalcogenide Glass Synthesis and Preparation of Preform 36

4.1 Rod-in-tube Approach for Production of Step-index Glass Preforms 37

4.2 Preform Design 39

4.3 Preparation of Rod and Tube Chalcogenide Glasses 40

4.3.1 Batch Chemicals 42

4.3.2 Vacuuming and Sealing 42

4.3.3 Melting, Quenching and Rotational Casting 45

4.3.4 Optical Characterization 47

4.4 Polymer Jacket Preparation 51

4.4.1 Thin Polymer Film Rolling 51

4.4.2 Consolidation 53

5 Fabrication of Multicore Fiber 54

5.1 The Iterative Size Reduction Method 56

5.2 Preliminary Test 58

5.3 Results and Discussion 60

5.3.1 First Step Drawing 62

5.3.2 Second Step Drawing 63

5.3.3 Third Step Drawing 63

6 Conclusion and Future Works 69

List of Figures

2.1 The schematic representation for symmetrized SSFM. In this approach fiber length is divided into segments of width h. The effect of the nonlinearity is taken into consideration at midpoints of the segments and the effect of the dispersion is calculated at the edges. 11

2.2 SPM induced a) phase shift b) frequency shift for Gaussian pulse [1]. 13

2.3 The calculated effect of SPM on spectral domain for a Gaussian pulse The GVD is neglected [1]. 14

2.4 Numerical calculations of supercontinuum generation and temporal change in 15 cm silica PCF with wavelengths (a) 600, (b) 670, (c) 720 nm and (d) 780 nm . The duration is 30 fs and peak power is 10kW. The line at 780 nm shows ZDW for the simulated fiber. . 18

2.5 Transmittance of various glasses with thicknesses of 2 - 3 mm [2]. 20

3.1 Experimental results of SC generation at $\lambda_p = 6.3$ μ m (a) The dashed black curve is the input spectrum and the curve in red is the output SC spectrum after 8 cm long length fiber. (b) The SC spectrum with increasing input peak power. (c) The cross-section of the chalcogenide step index fiber used in the experiments with core $As_2Se_3 \sim 16$ μm diameter and cladding $Ge_{10}As_{23.4}Se_{66.6}$ and the calculated ZDW of the fiber is 5.83 μ m [3] 24

3.2 SEM images of seven-core PCF. (a) side view and (b) cross-section. Measured beam profiles (c) near field and (d) far field [4]. 26

3.3 (a) Schematic of step-index fiber. (b) The material refractive index profile of the fiber is calculated for a polymer ($n_{polymer}$ =1.65) embedded core (n_{core} =2.73) covered with a cladding ($n_{cladding}$ =2.61). 28

3.4 The hundreds of ChGs fiber fabricated by utilizing the iterative size reduction method (a) cross-sectional SEM of polymer fiber that contains hundreds of As_2Se_3 –PVDF core–shell and (b) hexagonal packing the core–shell nanowires. 29

3.5 Design of polymer (brownish) embedded seven-core step-index fiber which have high nonlinearity, high refractive index and low loss in MIR core (black) and cladding (grey) which have lower refractive index and low loss in MIR (a) cross-sectional view (b) side view. 30

3.6 The material refractive index profile of the designed seven-core fiber calculated at 1.55 μm wavelength. $n_{core} = 2.73$, $n_{cladding}$ =2.61 and $n_{polymer}$ =1.65. 31

3.7 Calculated dispersion parameter of As_2Se_3 core and $Ge_{10}As_{23}Se_{67}$ cladding fiber with respect to core diameter at pump wavelength of 1.55 μm. The core diameter/cladding diameter is fixed to 0.728. The blue line shows the material dispersion of bulk core material As_2Se_3. 32

3.8 Calculated single-mode profile of the single fiber from seven-core design defined in Section 3.2. The As_2Se_3 core diameter is 0.95 μm and the $Ge_{10}As_{23}Se_{67}$ cladding radius is 1.35 μm. The black circles show the boundaries of core and cladding. 33

3.9 Spectral and temporal evolution of SC inside highly nonlinear 15 cm-length of single fiber with As_2Se_3 core for different peak powers (a) 5 W, (b) 10 W, (c) 20W, and (d) 50 W. 35

4.1 A macroscopic preform (a) before and (b) (c) after fiber drawing. (b) the remaining part after drawing process and (c) is the first coming part in fiber drawing process. 37

4.2 Rod-in-tube approach for fabricating IR step-index preforms (a) glass rod preparation for core of fiber via (a-1) casting; (a-2) thermal drawing; (a-3) extrusion; and (a-4) hot press. (b) Glass tube preparation for cladding via (b-1) casting; (b-2) drilling; (b-3) extrusion; or (b-4) rotational casting [5]. 38

4.3 The design of our preform (a) schematic representation (b) after producing all components of the preform. 40

4.4 The glovebox used in batching chemicals to quartz ampoules. . . . 41

4.5 Typical vacuuming and sealing setup used for fabrication of ChGs in sealed quartz ampoule. 43

4.6 (a) Sealing of evacuated tubes under high vacuum. (b) The sealed tubes with the raw materials. 44

4.7 (a) rocking furnace used in melt process. (b) The melted ChG inside the evacuated quartz tube. 44

4.8 (a) The fabricated As_2Se_3 rod. (b) The quenching of the melted ChG in water. 46

4.9 The quartz tube with melted ChG installed and rotated by the rotator machine used for rotational casting 46

4.10 The $Ge_{10}As_{23}Se_{67}$ tube fabricated by rotational casting 47

4.11 The refractive indices of $Ag_4(As_{0.4}Se_{0.6})_{96}$ and $As_{40}S_{25}Se_{35}$ and the NA of the fiber will consists these materials as core and cladding respectively. 49

4.12 The refractive indices of As_2Se_3, $Ge_{10}As_{23}Se_{67}$, and the NA of the fiber will consists these materials as core and cladding respectively. 49

4.13 Extinction coefficients of the ChGs synthesized 50

4.14 A model that shows polymer rolling, consolidation and fiber drawing processes. 50

4.15 Preparation of the polymer jacket for consolidation. 52

4.16 Consolidation of polymer in an evacuated consolidation furnace. . 52

5.1 (a) Fiber tower used in this study. (b) The components of the fiber tower are shown schematically. 55

5.2 Typical DSC curve 56

5.3 The DSC measurements of As_2Se_3, PES, and PEI. 57

5.4 A schematic shows the iterative size reduction method. 57

5.5 The preliminary attempt of fiber drawing. (a) The materials inside the polymer did not soften and broke to pieces. (b) The photo of the $Ag_4(As_{0.4}Se_{0.6})_{96}$ before (right, shiny) and after (left, matte) drawing. 59

5.6 The DSC data of $Ag_4(As_{0.4}Se_{0.6})_{96}$. 59

5.7 The powder X-ray diffraction measurement of the $Ag_4(As_{0.4}Se_{0.6})_{96}$ drawn as preliminary test before (red) and after (black) the fiber drawing. The measurements show the material crystallized during the drawing process. 60

5.8 The DSC data of $Ge_{10}As_{23}Se_{67}$. The T_g is at approximately 180 ℃. 61

5.9 The preform was prepared for the first step drawing. 61

5.10 The optical microscopy images of cross-section of first step fiber (a) bright field, (b) dark field. The boundaries of cladding and polymer are obvious in the bright field image but it is not possible to distinguish the core. The boundary of between core and cladding becomes distinguishable in dark field image. 62

5.11 The micrograph of the second step fiber. The seven-core design described in Section 3.2 becomes apparent after second step drawing. 64

5.12 The preform was prepared for the third step fiber drawing. The second step fibers with seven-core structure were placed to another polymer tube to draw the third step fiber and to obtain the desired diameter. 65

5.13 Micrograph of the third step fiber. There are 34 seven-core-structure in one fiber. Any of them can be used to obtain SC generation with high output power. 66

5.14 The seven-core-structure shown in the rectangle named as A in Figure 5.13 67

5.15 The seven-core-structure shown in the rectangle named as B in Figure 5.13 68

List of Tables

2.1 Nonlinear refractive indexes of different chalcogenide glasses measured at 1.55 μm by Z-scan method 21

4.1 The raw material materials weighed and poured to quartz tube with given ID (inner diameter) and OD (outer diameter). 41

4.2 The rocking furnace temperatures for different materials. 45

Chapter 1

Introduction

A Supercontinuum generation is the dramatic spectral broadening of intense light pulses while propagating through a nonlinear medium. As a result, the spectrum becomes extreme broad and it may extend over two octaves. Supercontinuum generation has different applications in optical frequency metrology [6, 7, 8, 9], spectroscopy [10, 11], and optical coherent tomography [12, 13]. The first observation of Supercontinuum generation that was a 200 THz wide continuum in bulk glass was reported in 1970 [14, 15]. Then researcher have exploited a huge variety of nonlinear materials including solids [14, 15, 16, 17], liquids [18, 19], gases [20, 21]. Investigation of SC generation by using optical fibers became an attractive research area in 1980s and 1990s. After 2000, by the progresses on fabrication of microstructured optical fibers (MOFs) and photonic crystal fibers (PCFs) the use of optical fibers on SC generation becomes more popular. The spectral broadening and the shape of the resultant spectrum are subject to the parameters of material and the pump source such as nonlinear refractive index, dispersion, pump pulse duration, pump peak power, and pump wavelength [22].

Until today, various types of waveguides such as silica photonic crystal fibers [23, 24, 25], tapered fibers [26, 27], and chalcogenide optical fibers [3, 27, 28, 29] have been successfully used for Supercontinuum generation. The optical

fibers are significantly useful for Supercontinuum generation due to the possibility of engineering the modal area and dispersion, raising the interaction length of the light with the nonlinear medium, and flexibilities in fiber design.

Three main challenges come into prominence about Supercontinuum generation by using optical fibers

1. Maximizing the spectral broadening for different spectrum regions,
2. Minimizing the Supercontinuum generation input threshold power,
3. Maximizing the output power of Supercontinuum generation.

This thesis deals with the third challenge, which is extensively studied in silica photonic crystal fibers [30, 31, 32], in infrared region. The first studies on high output power Supercontinuum generation were conducted on single core fibers. Multicore PCFs were shown to be more promising than single core fibers for high power Supercontinuum generation [33, 4]. Seven-core silica photonic crystal fiber was pumped with pulses with picosecond pulses, the Supercontinuum output power record with 112 W covering the wavelength range from 500 nm to beyond 1.7 μm [34].

The highest spectral range of the high output power Supercontinuum generation experiments with a silica photonic crystal fiber is from 0.4 to 2.25 μm. The absorption of silica in infrared region obstructs the spectral broadening to longer wavelengths. Therefore, the emerging technologies in fabrication of tellurite, ZBLAN and chalcogenide glass fibers which have wider transmission window in infrared than silica are developed. Chalcogenide glasses are outstanding for Supercontinuum generation generation due to their high nonlinearity and transmittance in mid IR [35]. A study in 2014 using chalcogenide glass (As_2Se_3) which has 833 times higher refractive index than silica) fiber achieved an outstanding spectral broadening covering from 1.4 μm to 13.3 μm which means the entire fingerprint region [3].

In this thesis, we merged the seven-core structure inspired by the studies on

maximizing the output power of Supercontinuum generation by seven-core silica photonic crystal fiber [33, 4, 34] and the properties of the chalcogenide glasses. We designed and fabricated a new seven-core-structured fiber with chalcogenide core/ chalcogenide cladding step-index fiber embedded in polyetherimide (PEI) polymer matrix. We used As_2Se_3 as core and $Ge_{10}As_{23}Se_{67}$ as cladding. The core-cladding structure provides us control the numerical aperture of the fiber and enables light to efficiently coupling of the light into highly nonlinear core and the cladding separates the coupled light from the highly absorbent polymer index in infrared region [36]. We fabricated 34 pieces of the seven-core-structured fiber embedded in one fiber successfully.

The thesis is organized as follows; **Chapter 2** introduces propagation of light in nonlinear media and nonlinear optical effects that can contribute to Supercontinuum generation. This chapter also gives brief information about optical properties of chalcogenide glasses. **Chapter 3** describes the overall process of designing seven-core-structured fiber. This includes theoretical modeling of fiber dispersion, and Supercontinuum generation calculations by using split step Fourier method. **Chapter 4** gives the information about preparation of preform. This includes chalcogenide glass rod and tube fabrication and polymer jacket fabrication. **Chapter 5** contains the all process of fiber fabrication by thermally drawing. The process is carried out in three iterative step until reaching the desired fiber diameter. This thesis ends with concluding remarks in **Chapter 6**.

Chapter 2

Background

For decades light matter interaction is an attractive topic for scientists. Today it is very well understood that light can enable to make matter to oscillate on atomic or molecular level, which in turns re-emit light that interferes with the incident light. For all conditions, light is subjected to dispersion in optical fibers. Optical nonlinearities take a role when the intensity of incident light is above a certain threshold. Some of them are resulted by Kerr effect which is the instantaneous refractive index depends on frequency and intensity of the light. The light disperses the new frequencies and leads to generate new frequencies through the optical fiber due to *Kerr effect*, respectively.

This part is concentrating on the nonlinear effects involved in supercontinuum generation. Supercontinuum generation is generally a combined result of many nonlinear effects which occur simultaneously. Much of the nonlinear optical theories can be found in books [37, 38] and the review on SC generation [22].

2.1 Linear Propagation

Linear propagation in an optical fiber refers to the case which the intensity of light is not sufficient enough to trigger nonlinear effects. A waveguide can constrain

an electromagnetic field by creating proper physical boundaries. Single mode fiber achieves guiding the light into the core region with lower refractive index cladding. The mathematical description of an electric field propagating in the fundamental mode can be given as

$$E(r,t) = \hat{x}F(x,y)A(z,t)exp^{i(\beta_0 z - \omega_0 t)} \tag{2.1}$$

where the electric field $E(r,t)$ is linearly polarized along $\hat{x}$ direction, $F(x,y)$ is the transverse field distribution, $A(z,t)$ is the pulse envelope and β_0 is the propagation constant at pulse center frequency, ω_0.

2.1.1 Dispersion

Dispersion is an effect originated from the frequency dependence of the refractive index of dielectric materials and it results in the light pulse propagating through an optical fiber to disperse. In this thesis *dispersion* refers to chromatic dispersion to distinguish it from mode or intermodal dispersion. Dispersion consists both material and waveguide dispersion. Frequency dependence of bulk materials is called material dispersion and waveguide dispersion is caused by the effective index change resulted by mode confinement [39].

In nonlinear optics utilizing ultra-short pulses, dispersion has great importance. When an ultra-short pulse having a broad spectrum range of frequency propagates in dispersive material these frequencies experience a different refractive index, so for normal dispersion regime the pulse broadens in time. This causes reduction on magnitude of peak power of pulse and, as a result, the nonlinear responses decreases dependently. Electronic vibrations limit transmission wavelength at the short wavelengths and vibrational resonances leads to loss at the long wavelength. The transmission window of fused silica which is used in many optical applications spans from 200 to 3000 nm. Far from the medium resonances, the refractive index variation can be calculated using by the Sellmeier equation [37]:

$$n^2 = 1 + \sum_{j=1}^{m} \frac{B_j \omega_j^2}{\omega_j^2 - \omega^2} \tag{2.2}$$

where ω_j is the resonance frequency and B_j is the strength of the j^{th} resonance. The group velocity corresponds to a group index, given by [40]

$$n_g = \frac{c}{v_g} = n + \omega \frac{dn}{d\omega} \tag{2.3}$$

where c is speed of light in vacuum, v_g is the group velocity, n is the refractive index, ω is the angular frequency. The group velocity enhances the group velocity dispersion (GVD), given by

$$GVD = \frac{d^2\beta}{d\omega^2} \tag{2.4}$$

GVD is in units of s^2/m. β is the propagation constant and can be expanded in a Taylor series about the pulse central frequency, ω_0 as

$$\beta = \beta_0 + \beta_1(\omega - \omega_0) + \beta_2 \frac{1}{2}(\omega - \omega_0) + \dots \tag{2.5}$$

where β_n is the n^{th} derivative of β_n with respect to ω at ω_0. It follows that β_0 is β/ω_0, which is $1/v_p$ where v_p is phase velocity, β_1 is $1/v_g$ and β_2 is equal to GVD. There are also higher order β_2 coefficients which can be observe in extremely short pulse experiments. Normal and anomalous dispersion is observed when $\beta_2 > 0$ and $\beta_2 < 0$, respectively. In normal dispersion regime, high frequencies travel slower than low frequencies therefore it leads to a pulse broadening in time domain and in anomalous regime it is vice versa.

Dispersion can also be expressed by another parameter called dispersion parameter, D. The parameter D describes how a propagating pulse with a given bandwidth (in nm) will disperse in time (in ps) after propagation along the fiber (in km), the unit of the parameter is ps/nm/km and it is expressed by [37]

$$D = \frac{d\beta_1}{d\lambda} = \frac{-2\pi c}{\lambda^2}\beta_2 = \frac{-\lambda}{c}\frac{d^2n}{d\lambda^2} \tag{2.6}$$

where λ is the wavelength. Changing the fiber design can provide to shift in dispersion. Since material dispersion is related to material used it is hard to change the property of a certain material. By changing design of waveguide it enables tuning of total dispersion and shift it desired value for specific wavelength. In many researches and applications it is important to obtain a zero dispersion wavelength (ZDW) waveguide. Engineering fiber to ZDW cause less spread and for supercontinuum generation it is vital keeping peak power at high level along the optical fiber without spreading.

2.2 Nonlinear Propagation

Electromagnetic phenomenon is governed by Maxwell equation, to fully understand the propagation of light in an optical fiber we must begin with Maxwell's equation. These equations take the form

$$\nabla \times \mathbf{E} = \frac{-\nabla \mathbf{B}}{\nabla t}, \tag{2.7}$$

$$\nabla \times \mathbf{H} = \mathbf{J} + \frac{-\nabla \mathbf{D}}{\nabla t}, \tag{2.8}$$

$$\nabla \cdot \mathbf{D} = \rho_f, \tag{2.9}$$

$$\nabla \cdot \mathbf{B} = 0, \tag{2.10}$$

Where $\mathbf{E}$ and $\mathbf{H}$ are electric and magnetic field vectors, $\mathbf{D}$ and $\mathbf{B}$ are electric flux densities. $\mathbf{J}$ is the current density vector and ρ_f is the charge density. $\mathbf{J}$ and ρ_f represent the sources of electromagnetic field. In an optical fiber $\mathbf{J}$ and ρ_f both are equals to 0.

$\mathbf{D}$ and $\mathbf{B}$ resulted by corresponding electric and magnetic field propagating through the medium are related by given equations [41]

$$\mathbf{D} = \epsilon_0 \mathbf{E} + \mathbf{P} \tag{2.11}$$

$$\mathbf{B} = \mu_0 \mathbf{H} + \mathbf{M} \tag{2.12}$$

where, ϵ_0 and μ_0 are the vacuum permittivity and the vacuum permeability, respectively, $\mathbf{P}$ is the induced electric polarization vector and $\mathbf{M}$ is the induced magnetic polarization vector. Because optical fibers are nonmagnetic, $\mathbf{M}$ is equals to 0.

From Maxwell's equation one can deduct an electromagnetic field propagating in an isotropic medium where is no free charges must follow the wave equation [37]

$$\nabla \times \nabla \times \mathbf{E}(r,t) = \frac{-1}{c} \frac{\delta^2 \mathbf{E}(r,t)}{\delta t^2} - \mu_0 \frac{\delta^2 \mathbf{P}(r,t)}{\delta t^2} \tag{2.13}$$

In dielectric medium, high intensity electromagnetic field can make the motion of bound electrons anharmonic, which results in nonlinear responses and create new

frequencies. The induced electric polarization $\mathbf{P}(r,t)$ can be written in Taylor expansion as [37]

$$\mathbf{P}(r,t) = \epsilon_0(\chi^{(1)} + \chi^{(2)}\mathbf{E}(r,t) + \chi^{(3)}\mathbf{E}(r,t)\mathbf{E}(r,t) + ...)\mathbf{E}(r,t) \tag{2.14}$$

where $\chi^{(n)}$ is the n^{th} order nonlinear susceptibility. Generally, $\chi^{(1)}$ suppresses the others effects. Its real part describes the refractive index and imaginary part describes the attenuation.

The lowest order nonlinear effects which are observable in the presence of high intensity electric field are related with $\chi^{(3)}$, which leads to Kerr effect and Raman scattering. Also the intensity related change in refractive index is also governed by $\chi^{(1)}$. Self modulation in refractive index dependent on intensity triggers phenomena such as self-phase modulation (SPM), cross-phase modulation (XPM) and four-wave mixing (FWM) which will be discussed later. The intensity dependent can be described as

$$\Delta n = n_2|E|^2; n_2 = \frac{3}{8n}Re(\chi^{(3)}_{xxxx}), \tag{2.15}$$

where $|E|^2$ is the optical intensity, Re indicates the real part. For symmetry reasons only $\chi^{(3)}_{xxxx}$ component of $\chi^{(3)}$ is non-zero for a linearly polarized field. Optical nonlinearities can be labelled by nonlinear refractive index.

Generalized nonlinear Schrödinger equation (GNLSE) can be derived for the pulse envelope, A, from Equation 2.13. The nonlinearity is assumed very low here and the bandwidth is less than less than $\approx 1/3$ of the carrier frequency. The GNLSE is concluded as [42].

$$\frac{\delta A}{\delta z} = i\sum_{m\geq 2}\frac{i^m\beta^m}{m!}\frac{\delta^m A}{\delta\tau^m} - \frac{\alpha}{2}A + i\gamma(1+\tau_{shock}\frac{\delta}{\delta\tau})(A(z,\tau)\int_{-\infty}^{\infty}R(\tau')|A(z,\tau-(\tau)')|^2 d\tau') \tag{2.16}$$

where $\tau = t - z/v_g$ and is called as retarded time frame. $|A(z,t)|^2$ is the instantaneous power. The first term of the right side is dispersion term, the second term corresponds to loss and the last term is the nonlinear term. The nonlinear coefficient,

$$\gamma = \frac{n_2(\omega_0)\omega_0}{cA_{eff}} \tag{2.17}$$

where A_{eff} is the effective modal area. For Gaussian pulses

$$A_{eff} = \pi w^2 \tag{2.18}$$

and

$$\frac{w}{a} = 0,65 + 1,619V^{-3/2} + 2.879V^{-6} \tag{2.19}$$

where a is the core radius and V is given by

$$V = \frac{2\pi}{\lambda} a \sqrt{(n_1^2 - n_c^2}} \tag{2.20}$$

n_1 is the core refractive index and n_c is the cladding refractive index.

The time derivative in 2.16 is described as $\tau_{shock} = 1/\omega_0$. Self-steepening is pioneered by this parameter and can be written as [37]

$$R(t) = (1 - f_R)\delta(\tau) + f_R h_R(\tau) \tag{2.21}$$

where $\delta(t)$ is the instantaneous electric response and $h_R(t)$ is the delayed Raman response. f_R is the relative strength of the *Kerr effect* and Raman response.

The standard nonlinear Schrödinger equation (NLSE) can be obtained by neglecting all parameters except nonlinear Kerr parameter and GVD. NLSE is the simplest form when studying 3^{th} order nonlinear susceptibility, $\chi^{(3)}$. It can be stated as [37]

$$\frac{\delta A}{\delta z} = -i\frac{\beta_2}{2}\frac{\delta^2 A}{\delta \tau^2} + i\gamma A|A|^2 \tag{2.22}$$

The generalized nonlinear Schrödinger equation (GNLSE) can be stated as 2.23

$$\frac{\delta A}{\delta z} = -i\frac{\beta_2}{2}\frac{\delta^2}{\delta \tau^2}A + \frac{\beta_3}{6}\frac{\delta^3}{\delta \tau^3} - \frac{\alpha}{2}A + i\gamma(|A|^2 + \frac{i}{\omega_0}\frac{1}{A}\frac{\delta}{\delta \tau}(|A|^2 A))A - T_R\frac{\delta |A|^2}{\delta \tau}A \tag{2.23}$$

2.2.1 Numerical Solutions

Except for some specific cases, the NLSE 2.22 does not contain analytical solutions. Many numerical approaches have been improved to provide a better understanding of how light propagates in a nonlinear fiber and the nonlinear responses [43, 44, 45, 46, 47, 48, 49, 50, 51]. Some of the numerical methods are

finite difference and the others are pseudospectral. The spectral methods are faster than finite difference methods up to some order of magnitudes and give very accurate results with nearly same accuracy [51]. One of the methods is finite difference time domain (FDTD) method which solves Maxwell's equations (in differential form) by splitting time and space into Yee grids [52]. The FDTD method is not further explained in this thesis. More extensively utilized method and very fast method rather than finite difference method is split step Fourier method (SSFM).

2.2.2 Split-Step Fourier Method

To understand the SSFM algorithm, 2.23 can be simplified as

$$\frac{\delta A}{\delta z}(\widehat{D}+\widehat{N})A \tag{2.24}$$

where $\widehat{D}$ is a differential operator and $\widehat{N}$ is a nonlinear operator. $\widehat{D}$ operator is responsible for dispersion and losses in assumed linear medium and $\widehat{N}$ operator consists nonlinear terms and governs nonlinearity. The explicit form of these operators can be written as [37]

$$\widehat{D} = -i\frac{\beta_2}{2}\frac{\delta^2}{\delta\tau^2} + \frac{\beta_3}{6}\frac{\delta^3}{\delta\tau^3} - \frac{\alpha}{2} \tag{2.25}$$

$$\widehat{N} = i\gamma(|A|^2 + \frac{i}{\omega_0}\frac{1}{A}\frac{\delta}{\delta\tau}(|A|^2A)) - T_R\frac{\delta|A|^2}{\delta\tau} \tag{2.26}$$

where $T = \tau$ which is given before. The SSFM present a simple solution of for NLSE by propagating the pulse envelope for a small distance . In this method the nonlinear and dispersion assumed to behave not interacting with each other when they propagate from z to $z+h$. The propagation is carried out in two step, in the first one $\widehat{D}$ is assumed to be zero, the pulse is affected by linearity only and in the second step $\widehat{N}$ is assumed to be zero, the pulse is affected by only the dispersion. It can be given by [37]

$$A(z+h,\tau) \approx exp(h\widehat{D})exp(h\widehat{N})A(z,\tau) \tag{2.27}$$

The term $exp(h\widehat{D})$ can be calculated in the Fourier transform Domain as

$$exp(h\widehat{D})B(z,T) = F_T^{-1}exp[h\widehat{D})(-i\omega)]F_TB(z,T) \tag{2.28}$$

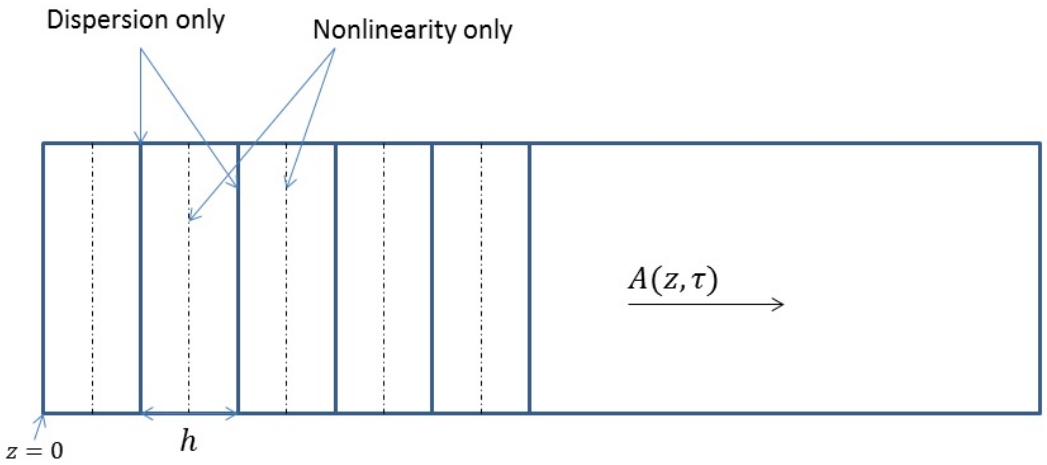

Figure 2.1: The schematic representation for symmetrized SSFM. In this approach fiber length is divided into segments of width h. The effect of the nonlinearity is taken into consideration at midpoints of the segments and the effect of the dispersion is calculated at the edges.

where F_T indicates the Fourier transform operation and $\widehat{D}(-i\omega)$ can be deducted from 2.23 by writing $-i\omega$ instead of $\frac{\delta}{\delta\tau}$, and ω is the frequency in the Fourier domain. Different approaches can be applied to increase the accuracy of the SSFM. In one procedure 2.27 is replaced by [53, 37]

$$A(z+h) \approx exp(\frac{h}{2}\widehat{D})exp(\int_z^{z+h} \widehat{N}(z')dz')exp(\frac{h}{2}\widehat{D})A(z,\tau) \tag{2.29}$$

In here the effect of nonlinearity is taken into account into the middle of the segment from z to $z+h$. This equation is called symmetrized SSFM and it provides more accurate results. The middle term can be simplified by approximation of the integral such as [37]

$$\int_z^{z+h} \widehat{N}(z')dz' \approx \frac{h}{2}[\widehat{N}(z) + \widehat{N}(z+h)] \tag{2.30}$$

2.2.3 Optical Kerr Effect

The refractive index of a material is dependent on the intensity of incidence light. The phenomenon is called as Kerr effect. This effect is firstly observed in optical

fiber in 1973 [54]. The instantaneous interactions between the material and light cause a change in the refractive index. For a low intensity the effect can be neglectable for most cases but the change is more observable when the intensity of the light is adequately high such as very intense laser beam. The Kerr effect can be written as

$$n(I) = n_0 + n_2 I \tag{2.31}$$

The nonlinear coefficient n_2 can be written in terms of the third order susceptibility as [37] in Equation 2.15. The index variation caused by Kerr effect leads to nonlinear optical effects of self-phase modulation (SPM), cross phase modulation (XPM), and modulation instability. Third harmonic generation and Four wave mixing (FWM) can be significant if the phase matching conditions are satisfied [37].

2.2.4 Self-Phase Modulation

The *Kerr effect* leads variation on phase velocity which means the phase velocity becomes intensity dependent. This variation results in SPM of a propagating pulse [55]. By neglecting the dispersion parameter (GVD) $\beta_2 = 0$ SPM can be easily observed from 2.22 which has the general solution in a fiber with length L [37]

$$A(L,t) = A(0,t)exp(i\phi_{NL}(L,t)) \tag{2.32}$$

$$\phi_{NL}(L,t) = \frac{n_2 I(t)\omega_0 L}{c} \tag{2.33}$$

The time dependent change in phase ϕ_{NL} leads to the SPM induced broadening in spectral domain. If the frequency of the incident light is described as

$$\omega(t) = \omega(0) + \delta\omega(t) \tag{2.34}$$

The difference $\delta\omega(t)$ becomes

$$\delta\omega(t) = -\frac{\delta\phi_{NL}}{\delta t} = -\frac{n_2\omega_0 L}{c}\frac{\delta I(t)}{\delta t} \tag{2.35}$$

where $I(t) = I_0|U(t)|^2$ and $|U(t)|$ is the normalized amplitude,

$$\delta\omega(t) = -\frac{n_2\omega_0 L}{c} I_0 \frac{\delta|U(t)|^2}{\delta t} \tag{2.36}$$

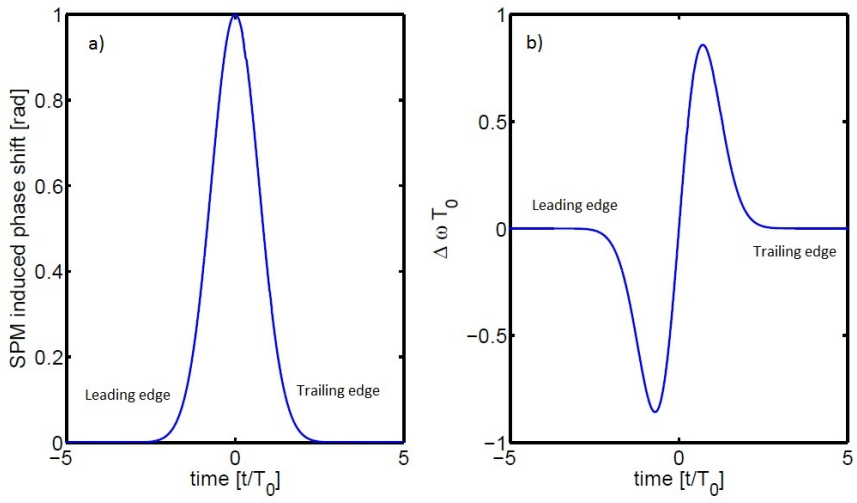

Figure 2.2: SPM induced a) phase shift b) frequency shift for Gaussian pulse [1].

then $\delta\omega(t)$ becomes

$$\delta\omega(t) = -\frac{L}{L_{NL}}\frac{\delta|U(t)|^2}{\delta t} \tag{2.37}$$

where L_{NL} is the nonlinear length stated as

$$L_{NL} = \frac{1}{\gamma P_0} \tag{2.38}$$

where the peak power is

$$P_0 = I_0 A_{eff} \tag{2.39}$$

and the nonlinear coefficient is

$$\gamma = \frac{n_2\omega_0}{cA_{eff}} \tag{2.40}$$

The time dependent $\delta\omega(t)$ is called as frequency chirp. The time dependent phase shift $(\phi_{NL}(z,t))$ leads to spectral changes; for an unchirped Gaussian pulse, the leading edge will be downshifted and the trailing one will be upshifted as shown in Figure 2.2

Figure 2.2 shows the nonlinear phase and frequency shift induced by SPM for a Gaussian pulse. For the trailing edge there is a positive frequency shift therefore it generates shorter wavelengths and for the leading part it is vice versa. Figure

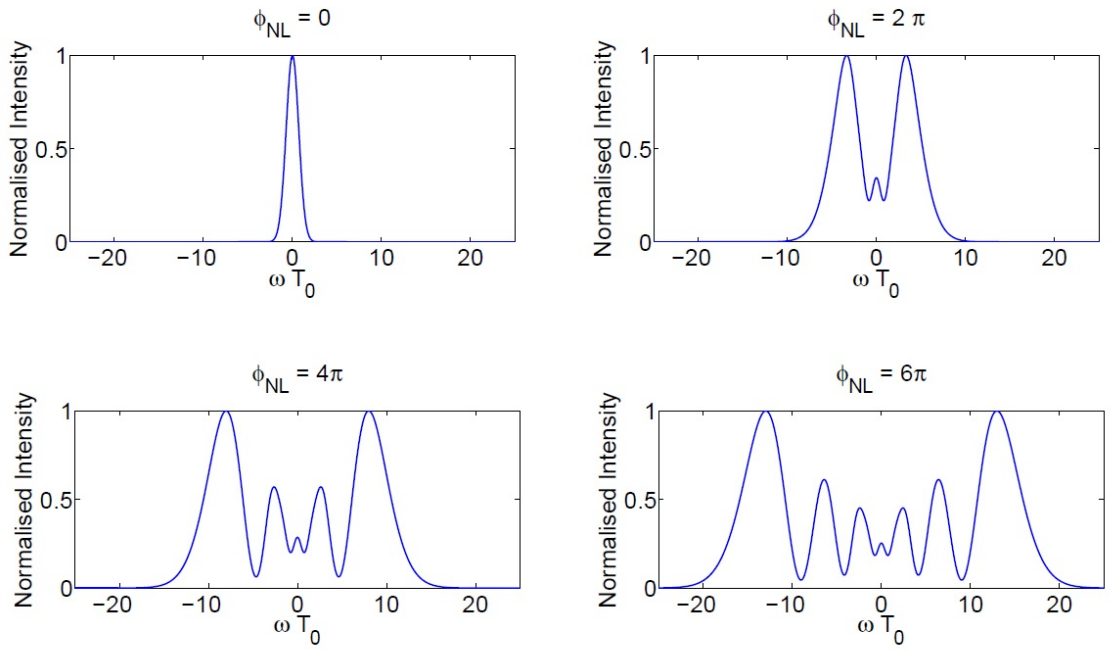

Figure 2.3: The calculated effect of SPM on spectral domain for a Gaussian pulse The GVD is neglected [1].

2.3 shows the generated spectrum with respect to different phase shifts while there is no dispersion. It is apparent the spectrum broadens symmetrically.

2.2.5 Cross Phase Modulation

Due to the Kerr effect the refractive index of a material can be shifted by a intense co-propagating light through XPM. To understand the nature of it the total electric field **E** in 2.14 can be written as [37]

$$\mathbf{E} = \frac{1}{2}\hat{x}[E_1 exp(-i\omega_1 t) + E_2 exp(-i\omega_2 t) + c.c.] \tag{2.41}$$

where the electric fields with frequencies ω_1 and ω_2 propagate simultaneously inside an optical fiber and polarized along the x-axis. The *c.c.* refers to the complex conjugates of the electric fields. The nonlinear phase shift experienced by the electric field E_1 while the electric fields E_1 and E_2 propagate at the same

time with different frequencies can be approximated by [37]

$$\phi_{NL} = n_2 k_0 L(|E_1|^2 + 2|E_2|^2) \tag{2.42}$$

and it is similar for the phase shift of E_2. The terms at the right hand side of the equations refer to SPM and XPM, respectively. By an easy deduction from the equation, it is obvious that for equally intense electric fields of different frequencies the contribution of XPM to the nonlinear phase shift is double of SPM. If it is assumed there is no XPM and SPM acts alone, the spectral broadening is symmetric. For different intensities of co-propagating waves the spectral broadening is asymmetric due to XPM.

2.2.6 Four Wave Mixing

The nonlinear processes can be called as second- or third-order parametric processes if they are related to $\chi^{(2)}$ and $\chi^{(3)}$ respectively. Four wave mixing (FWM) is a third order parametric process due to the nonlinear interaction of four frequencies that mix and generate new frequencies. In this process the photon energy is not transferred to medium. The mixing occurs in a way that the energy and momentum conservation is fulfilled [37, 56, 57].

A clear FWM can be observed when the phase matching conditions are nearly satisfied. The phase matching conditions implies that the matching of frequencies and in addition to that the matching of the wave vectors of the interacting waves. For higher efficiency of FWM, the input frequency and fiber parameters can be chosen particularly to satisfy the phase matching conditions.

There are two types of FWM [37]. In the first case, there are three photons mixing and transferring their energy to a new photon generated at frequency $\omega_4 = \omega_1 + \omega_2 + \omega_3$. The third-harmonic generation is the special case when the mixed three waves equal to each other as $\omega_1 = \omega_2 = \omega_3$. When $\omega_1 = \omega_2 \neq \omega_3$, then, it is named as frequency conversion. In the second case, two photons at frequencies of ω_1 and ω_2 are mixed and anhiliated to generate two different photons at frequencies of ω_1 and ω_2 which satisfies the condition $\omega_1 + \omega_2 = \omega_3 + \omega_4$.

The wave vectors of the interacting waves need to be matched as

$$k_4 = k_1 + k_2 + k_3 \tag{2.43}$$

$$k_3 + k_4 = k_1 + k_2 \tag{2.44}$$

for the first and second cases respectively.

FWM has a significant contribution to the Supercontinuum generation especially for pulses with the order of picoseconds duration. It is significant for the anomalous dispersion regime but it can be observed in normal dispersion regime with low efficiency.

2.2.7 Stimulated Raman Scattering

While the electronic responses provoking the Kerr nonlinearities are instantaneous, stimulated Raman scattering (SRS) is a non-instantaneous third-order nonlinear susceptibility process. SRS is an inelastic scattering process and there is an energy transfer from a photon to a phonon or vice versa if the requirements are satisfied. Also it is a non-parametric nonlinear process due to the imaginary part of $\chi^{(3)}$.

In spontaneous Raman scattering, new frequencies are generated because of energy transfers between photons and phonons. If a photon transfers some of its energy to a phonon the frequency will be downshifted and if a phonon transfers some of its energy to a photon the frequency will be upshifted. The wave generated in the first case is called as Stokes wave and in the second one is called as anti-Stokes. The second case occurs more frequently as it requires a phonon of the right energy and momentum. It is possible to convert up to 10% of the pump light to Stokes wave by efficient SRS in the case of intense laser beam pumping.

2.3 Supercontinuum Generation

New frequencies can be generated by all nonlinear processes. For high intense power the nonlinear responses can occur at the same time and generate new frequencies which cause a broadening in spectral domain. As a result the spectrum so broad it may extend over two octaves. Such extreme spectral broadening is named as Supercontinuum (SC) generation. SC generation first observed in 1970s in solid and gaseous media by Alfano and Shapira [14, 15]. Later SC is investigated by Lin in 1976 in optical fiber by using 10 ns pulses [58]. Investigation of SC generation by using optical fibers became an attractive research area in 1980s and 1990s. After 2000, by the progresses on fabrication of microstructured optical fibers (MOFs) and photonic crystal fibers (PCFs) the use of optical fibers on SC generation become more popular, and some reviews appeared in literature on this topic [22, 59, 60, 61].

While SC generation takes places many nonlinear effects may occur at the same time, such as SPM, XPM, SRS, FWM and so on. Depending of the parameters of input pulse (pulse duration, width, peak power, wavelength) and material properties (dispersion and nonlinearity) the dominating nonlinear effect can be changed. SPM and SRS are the leading nonlinear optical mechanisms when the pump wavelength shorter than zero dispersion wavelength (ZDW) since solitons cannot form. These first experiments in SC generation were conducted in the normal dispersion regime therefore SRS and SPM was the dominating reason for the SC generation.

In normal dispersion regime, SPM and dispersion cause a very fast spreading in the temporal domain and prevent a broad SC generated by soliton dynamics. If broadened wavelengths reach up to ZDW and exceed to the anomalous regime than they will be affected by the Solitonic effects and cause more broadening in spectrum. Fig SC1 shows the evolution of SC generation and temporal change while propagating through 15 cm silica PCF for the pump wavelengths of (a) 600, (b) 670 (c) 720 and (d) 780 nm. Figure 2.4 (d) shows the output spectrum for different wavelengths. The nonlinear parameter γ is 1.1 $W^{-1}m^{-1}$. In Figure 2.4

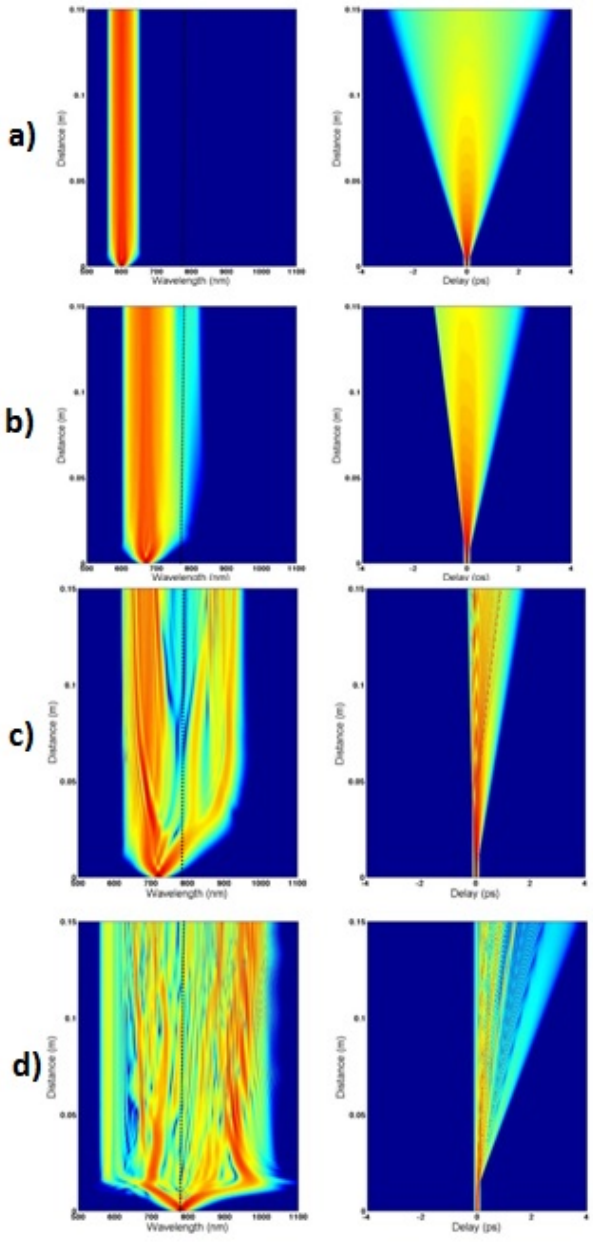

Figure 2.4: Numerical calculations of supercontinuum generation and temporal change in 15 cm silica PCF with wavelengths (a) 600, (b) 670, (c) 720 nm and (d) 780 nm . The duration is 30 fs and peak power is 10kW. The line at 780 nm shows ZDW for the simulated fiber.

(a), for 600 nm pump wavelength the broadening at the beginning is governed by SPM and there is no broadening after a few millimetres since the high dispersion. The peak power is drastically diminished by the high dispersion. For the 670 nm pump wavelength in Figure 2.4 (b) the broadening is dominated by SPM and the pulse affected by normal dispersion. This causes a rapid temporal expansion of pulse and decrease the peak power dramatically at the very beginning of the fiber. The figure shows the limited broadening in the normal dispersion because it is governed by SPM dominantly and there is no Solitonic contribution. Raman effects also play role in the shape of the spectrum. In Figure 2.4 (c) the pump wavelength is 720 nm and closer to the fiber ZDW. In this situation some of the pulse energy is transferred to the anomalous dispersion regime. In the normal dispersion regime SPM dominates the broadening and in the anomalous dispersion regime solitonic effects has a significant effect in broadening. The other nonlinear effects may have a role in broadening and oscillation but here it is not obvious to investigate. For the pump wavelength of 780 nm which is the ZDW shown in Figure 2.4 (d) it is obvious that the solitonic effects have great dominancy on the spectral broadening.

2.4 Chalcogenide Glasses

Chalcogenides glasses (ChGs) include the one or more of Group 6a elements excluding oxygen that are known as chalcogens (S, Se, and Te). They are formed by addition of other elements like As, Sb, Ge, Ga, P, Zn, and so on. ChGs are semiconductors which have usage in phase-change memories, sensors [62] and recently ChGs became popular in photonics due to their transmittance in the near and mid infrared and their low phonon energies provides to dope them with rare earth dopants [63, 64, 65] which enables to change the optical properties of the ChGs. The heaviness of the atoms forming the ChGs results in low vibrational energies in bonds. This makes the ChGs to have a great transmittance in mid infrared. Sulphides, selenides and tellurides transmit infrared light up to ~ 12, ~ 16 and ~ 20 μm, respectively as shown in Figure 2.5. The glass transition temperatures of ChGs are low due to the weak covalent bonding, thus, glass

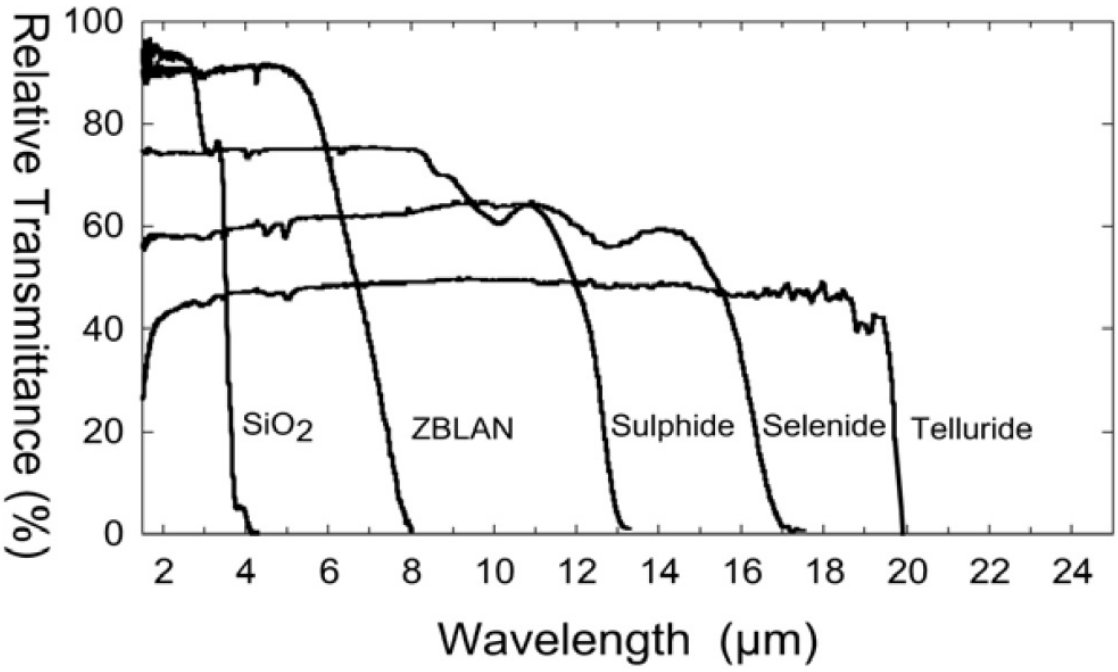

Figure 2.5: Transmittance of various glasses with thicknesses of 2 - 3 mm [2].

moulding is a feasible method for glass fabrication of optical applications such as thermal imaging [66, 63, 67], supercontinuum generation [3, 68] and chalcogenide fiber drawing [69, 70]. ChGs have higher glass densities when comparing to oxide glasses, this results in to high refractive index approximately between 2 and 3. Miller's rule [71] refers to that when the linear refractive index is high, nonlinear refractive index is high as experiments has been verified [72, 73].

Researches showed that nonlinear coefficients of ChGs can reach up to thousand times of nonlinear coefficient of silica glass as show in Table 4.1. Therefore chalcogenides are very attractive for supercontinuum generation [27, 3, 68, 28, 79, 80, 81, 82].

Table 2.1: Nonlinear refractive indexes of different chalcogenide glasses measured at 1.55 μm by Z-scan method

Material	$n_2(m^2W^{-1})$	$n_2/n_{2,fusedsilica}$
$Ag_4(As_{0.4}Se_{0.6})_{96}$ [74]	6.05×10^{-17}	2190
As_2Se_3 [73]	2.3×10^{-17}	833
$As_{25}S_{55}Te_{20}$ [73]	1.16×10^{-17}	420
$As_{40}S_{30}Se_{30}$ [73]	1.1×10^{-17}	400
As_2S_3 [73]	5.4×10^{-18}	195
Tellurite glass [75]	5.9×10^{-19}	21
Bismuth silicate glass [76]	3.2×10^{-19}	12
Fused Silica [77]	2.76×10^{-20}	1
ZBLAN [78]	2.2×10^{-20}	0.8

Chapter 3

New Fiber Design for High Supercontinuum Generation Output Power in Mid Infrared

3.1 Supercontinuum Generation in Optical Fibers

The demonstration of SC generation with using silica PCF [23] and silica tapers [26] became attractive more than a decade ago. Silica has high absorption in mid IR region and this have provoked the progress in fabrication of telluride, ZBLAN and chalcogenide glass fibers which have low loss in fingerprint region. For instance a SC spanning from 1 μm to 5 μm is generated by using 8 mm long highly nonlinear microstructured telluride PCF at 1.55 μm pump wavelength with peak power P_p=17 kW and the pulse duration τ_p=110 fs [83] and SC between 1.9 μm and 4.5 μm is obtained by 8.5 m long ZBLAN at 2 μm pump wavelength with P_p =16 kW nanosecond pulses [84]. The fiber absorptions beyond 4 μm obstruct the broadening of the SC. The SC can be extending to longer wavelengths by using relatively short fiber length and high P_p. 2 cm ZBLAN fiber is pumped

at 1.45 m with P_p=50 MW and the pulse duration τ_p =180 fs, then, the SC is extended up to 6.8 μm [85].

Recently SC generation is observed in chalcogenide fibers. ChGs are outstanding for SC generation due to their high nonlinearity and transmittance in mid IR [35]. In chalcogenide glasses high GVD is a problem for SC generation in ChGs fibers. Recent studies showed engineering of their GVD is possible by engineering of fiber radiuses. One-octave spanning (850 nm to 2.35 μm) SC is shown in 5 cm long nanotaper with a minimum 480 nm diameter at 1.55 μm pump wavelength with τ_p=1 ps and P_p =3.5 kW [28]. A SC spanning from 1 μm to 2.6 μm is obtained by using 30 cm long As_2S_3 fiber at 1.55 μm with τ_p=400 fs and P_p =5.6 kW [29].

3.1.1 Challenges in Supercontinuum Generation with Optical Fibers

The studies on supercontinuum generation exploiting optical fibers are focused on 3 main challenges as

1. Maximizing the spectral SC broadening for different spectrum regions
2. Minimizing the SC generation input threshold power
3. Maximizing the output power of SC

For the first challenge the studies talked until now are descent examples for the solution of this challenge. The recent studies showed valuable progresses to solve this issue. For example, SC covers deep ultraviolet region starting from 200 nm up to 2.5 μm which means more than 3 octave spanning SC was achieved using a 1 μm diameter junction of a ZBLAN PCF where pump wavelength λ_p =1042 nm, τ_p =140 fs, and P_p =5.9 kW [86]. In this experiment the size of the junction is engineered to have ZDW at $\sim$ 1040 nm. The one of the most vital result of this study is the SC generation which is stable in the UV region however

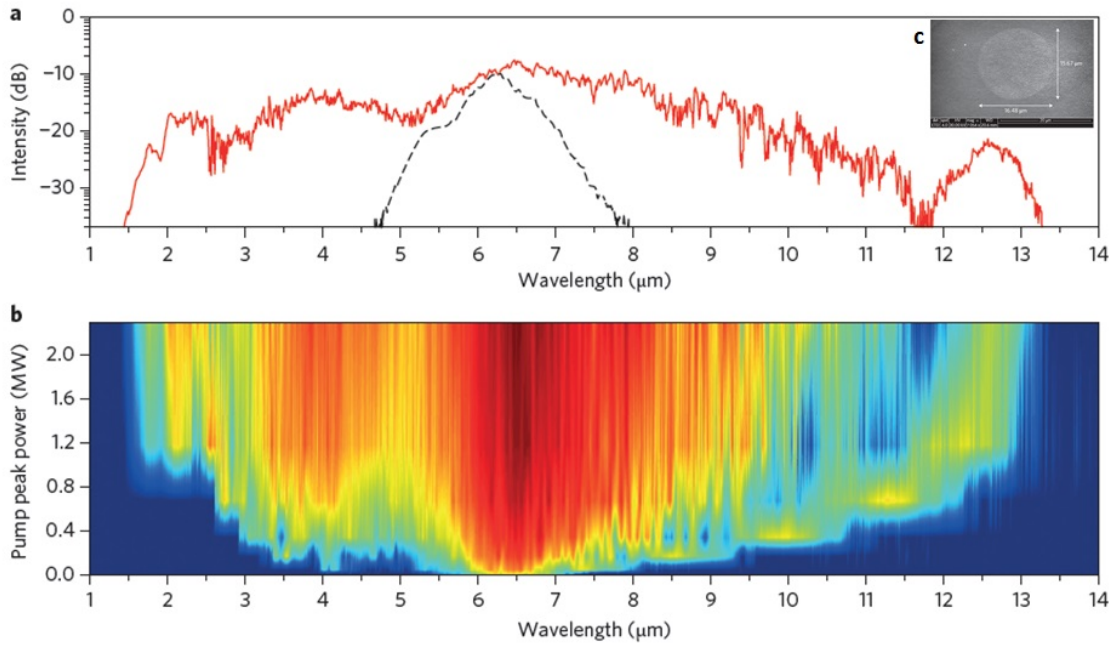

Figure 3.1: Experimental results of SC generation at $\lambda_p = 6.3$ μ m (a) The dashed black curve is the input spectrum and the curve in red is the output SC spectrum after 8 cm long length fiber. (b) The SC spectrum with increasing input peak power. (c) The cross-section of the chalcogenide step index fiber used in the experiments with core $As_2Se_3 \sim 16$ μm diameter and cladding $Ge_{10}As_{23.4}Se_{66.6}$ and the calculated ZDW of the fiber is 5.83 μ m [3]

the light between 200 nm and 400 nm carries 10% of the total energy. No damage has been observed after 24 h hour pumping in this experiment

A study in 2014 shown in Figure 3.1 using ChGs fiber has a significant record on the spectral broadening in IR region [3]. The study achieved to obtain an utmost broad spectrum for a fiber from 1.4 μm to 13.3 μm which spans the entire fingerprint region. A chalcogenide step index fiber with core As_2Se_3 and cladding $Ge_{10}As_{23.4}Se_{66.6}$ is pumped with laser at λ_p =6.3 μm, τ_p =100 fs, and P_p =2.9 MW. The peak power used here is relatively high since the fiber is multimode instead of single mode fiber(SMF).

For the second challenge tapering is the most promising method for minimizing the threshold input power. For example, SC generation between 1.15 μm and 1.65

μm is shown in an As_2Se_3 taper with a very low peak power P_p=7.8 W at λ_p =1.55 μm and τ_p =250 fs [27]. ZDW of the wavelength is fixed to 1.55 μm for fiber diameter 1 μm. They used 22 cm-long taper with 3 cm submicrometer section. They also observed self-phase modulation with P_p =1.5 W. The reason for broadening in low power is the refractive index change in Equation 2.31 is dependent on the intensity of light. The efficient coupling of the most of the light to the submicrometer part of the taper by using tapering geometry raises the intensity of light inside the section and increases the nonlinear responses, therefore SC generation.

The third challenge is extensively studied in silica and doped silica PCF. The studies first began with single-core PCFs. The first example of high power SC generation with single-core silica PCF is published in 2003 and SC between 800 nm and 1.8 μm with the average power P_{avg} =5 W is obtained by using picosecond pulses [30]. Then SC spans from 1.2 μm to 1.8 μm with output P_{avg}=3.2 W is obtained with one core fluoride doped silica called as highly nonlinear dispersion shifted fiber (HNLF) which is pumped with continuous wave (CW) laser [31]. SC spanning 0.4-2.25 μm with output P_{avg}=39 W is obtained with 5.7 m-long silica PCF pumped with picosecond pulse [32]. The SC covers visible and the most of near infrared but broadening in longer wavelengths is obstructed due to the absorbance of the wavelengths longer than 2.4 μm. The common problem faced in single-core high power SC generation is damages occurring due to high pump intensity. The damage is occurred at the pumped facet of the fiber or inside the fiber. The damage occurs mostly at the thinnest part of the tapered fibers.

Multicore PCFs are promising for high power SC generation. SC spanning 0.5-1.7 with output P_{avg} =5.4 W μm is generated by using seven-core silica PCF [33]. The 20 m-long seven-core fiber is pump with femtosecond pulses. The results is important because picosecond pulses are mostly utilized in high power SC generation. Here they showed the capability of generating high power SC by utilizing seven-core fiber design. SC covering the wavelength range from 720 nm to beyond 1.7 μm with P_{avg} =42.3 W is generated by using seven-core fiber pumped with picosecond pulses [4]. 20 m-length of seven-core silica PCF shown in Figure 3.2 is pumped with pulses with τ_{avg} =20 ps. The SC output power

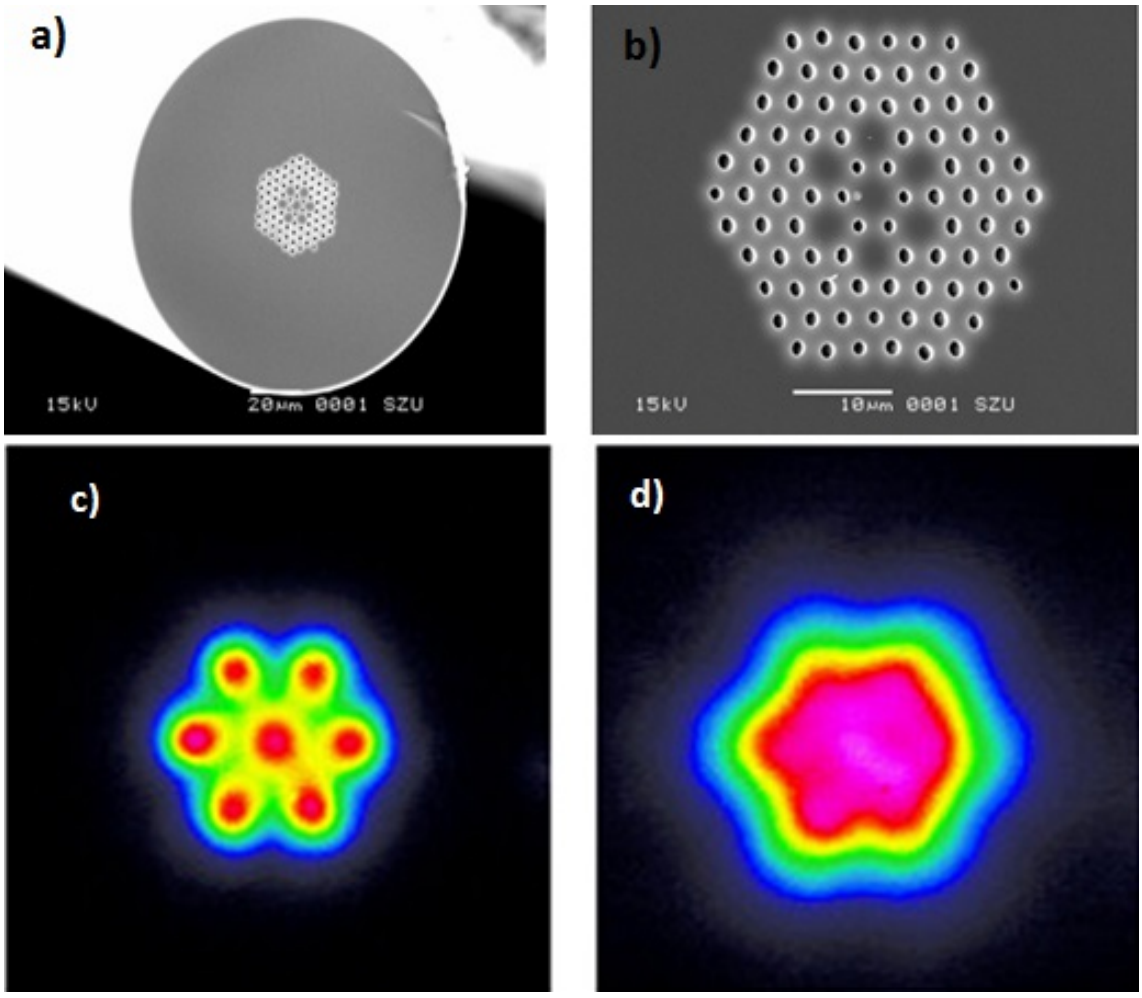

Figure 3.2: SEM images of seven-core PCF. (a) side view and (b) cross-section. Measured beam profiles (c) near field and (d) far field [4].

record with picosecond pulses is 112 W until now [34]. The obtained SC covers wavelength range from 500 nm to beyond 1.7 μm.

3.2 Design of Chalcogenide Core/Chalcogenide Cladding Step-Index Seven-Core fiber

Using silica or doped silica multicore fiber limits the range of generated SC. The SC generation does not reach to mid infrared because of fiber losses. The high power SC experiments achieved the best spanning spectrum range as 0.4-2.25 μm with output P_{avg} =39 W [32]. The ChGs fibers are promising for SC generation covers MIR and even entire fingerprint region. Multicore ChGs fibers can be used for high power SC generation in IR region. One of the best ways of fabricating multicore ChGs fiber with desired diameter which provides engineering the fiber ZDW is iterative size reduction (ISR) method [70] which will be described in detail at Chapter 5. Figure 3.4 shows the polymer embedded submicrometer ChGs fibers fabricated by ISR method. The hexagonal package shown in Figure 3.4 (b) gives us the desired geometry of seven-core PCFs used in high power SC generation shown in Figure 3.2(a), (b). One can pump the seven fibers by choosing which to pump.

The challenge of pumping polymer embedded ChGs fiber shown in Figure 3.4 is the high absorbance of the polymer covering the ChGs in infrared region [36]. Most of the pumped power is absorbed by the polymer. Therefore, to use this method efficiently for high power SC generation it is needed to separate with another material as cladding which have low loss in IR region. The best material for cladding is also ChGs due to their low loss in IR region. The cladding material has to have lower refractive index than our nonlinear core step-index fiber as shown in Figure 3.3 to provide coupling of light into the core.

Figure 3.5 shows our design for chalcogenide glass core (black) and different chalcogenide glass cladding (grey). They are embedded in a polymer jacket

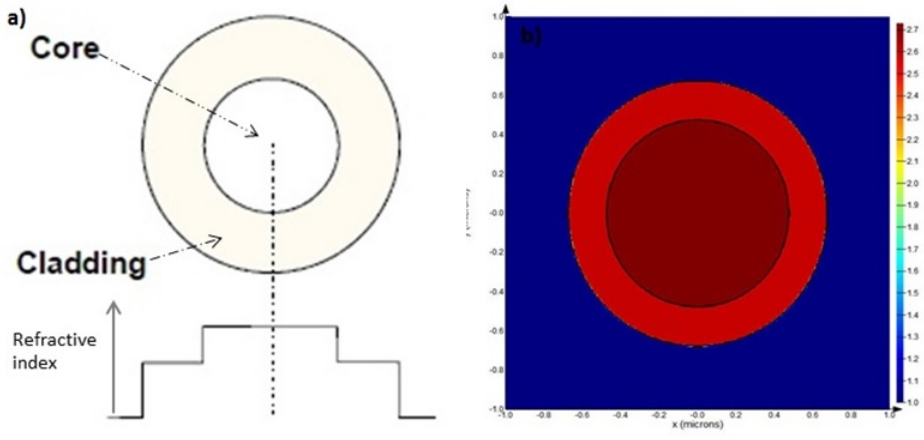

Figure 3.3: (a) Schematic of step-index fiber. (b) The material refractive index profile of the fiber is calculated for a polymer ($n_{polymer}$ =1.65) embedded core (n_{core} =2.73) covered with a cladding ($n_{cladding}$ =2.61).

(brownish). This fiber is easy to fabricate with ISR method. The seven-core design provides us to get more output SC power than single ChG core fiber.

The step-index structure show in Figure 3.6 of the fiber cores enables effective coupling of light into the core and separation of the light from the polymer jacket. This will reduced the loss due to the high absorption of polymer in MIR region. Seven-core design is inspired from the studies on high output power SC generation with seven-core PCFs which have the record output SC power. The core number can be easily raised by ISR method if it is necessary.

3.2.1 Dispersion Calculation

Dispersion parameter for our fiber is calculated by the help of commercially available Lumerical Mode Solution. The fiber is designed as As_2Se_3 core and $Ge_{10}As_{23}Se_{67}$ cladding with core diameter/cladding diameter is fixed at 0.728 which is selected since before drawing the fiber the As_2Se_3 rod had 7.5 mm diameter total, and $Ge_{10}As_{23}Se_{67}$ cladding material had 10.3 mm outer diameter.

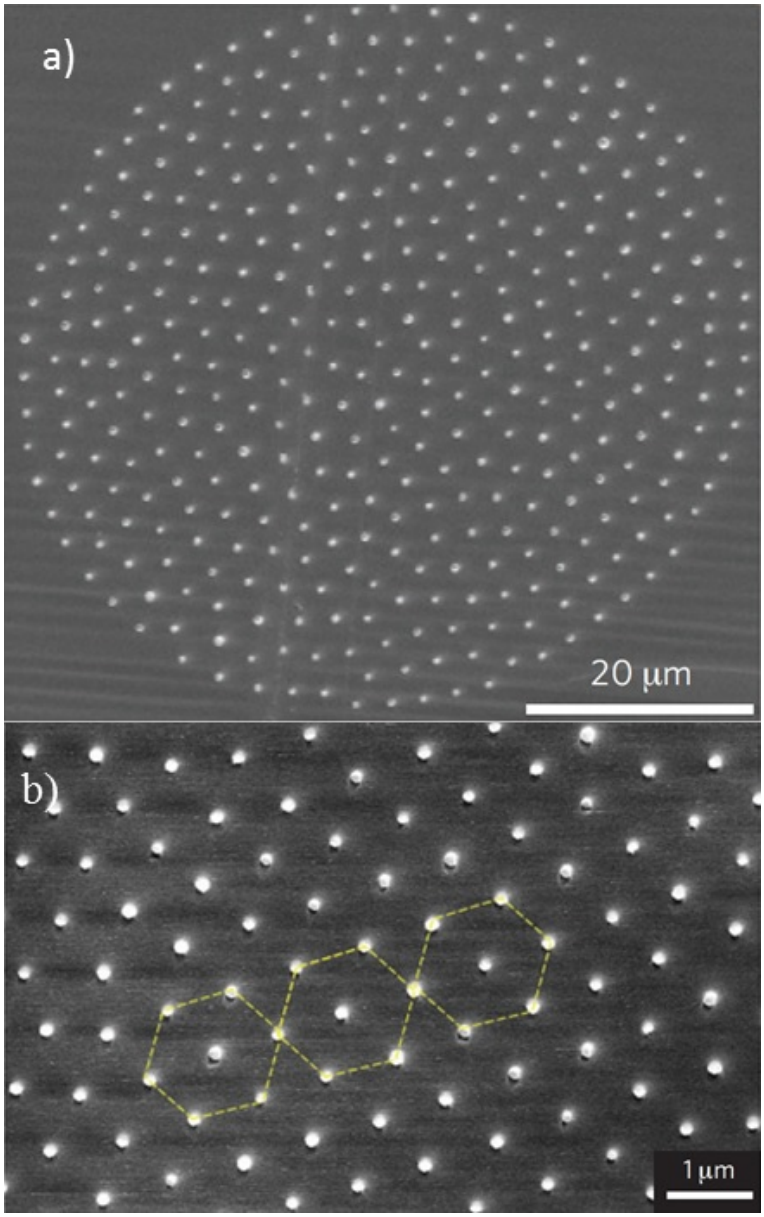

Figure 3.4: The hundreds of ChGs fiber fabricated by utilizing the iterative size reduction method (a) cross-sectional SEM of polymer fiber that contains hundreds of As_2Se_3 –PVDF core–shell and (b) hexagonal packing the core–shell nanowires.

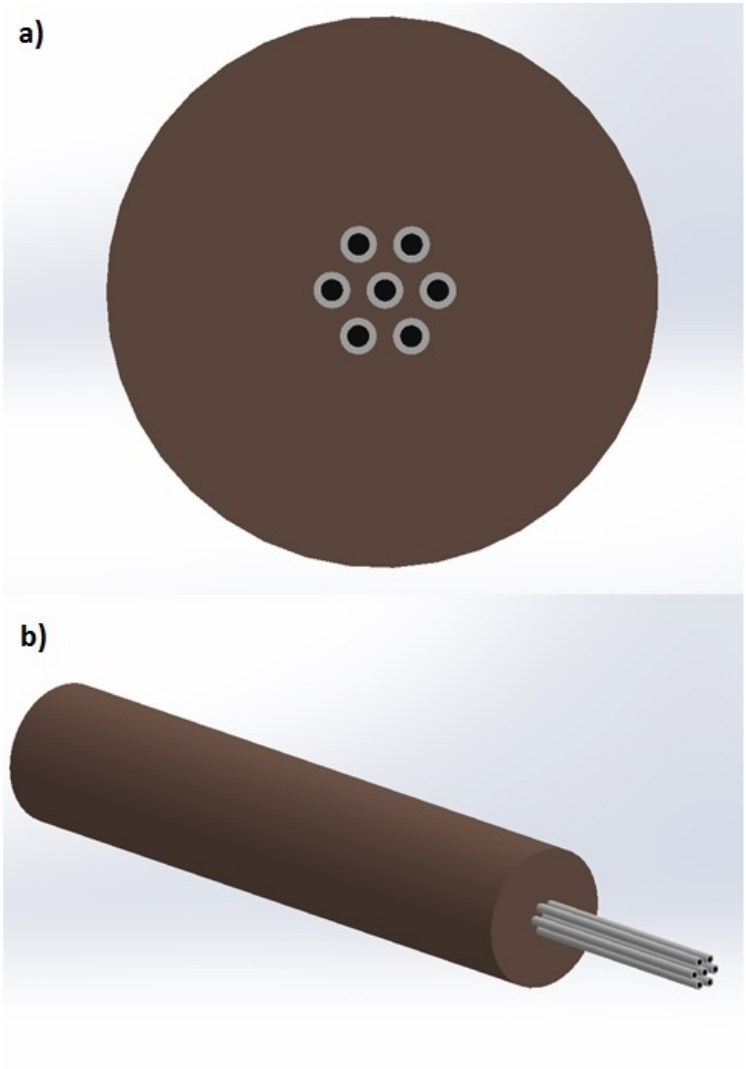

Figure 3.5: Design of polymer (brownish) embedded seven-core step-index fiber which have high nonlinearity, high refractive index and low loss in MIR core (black) and cladding (grey) which have lower refractive index and low loss in MIR (a) cross-sectional view (b) side view.

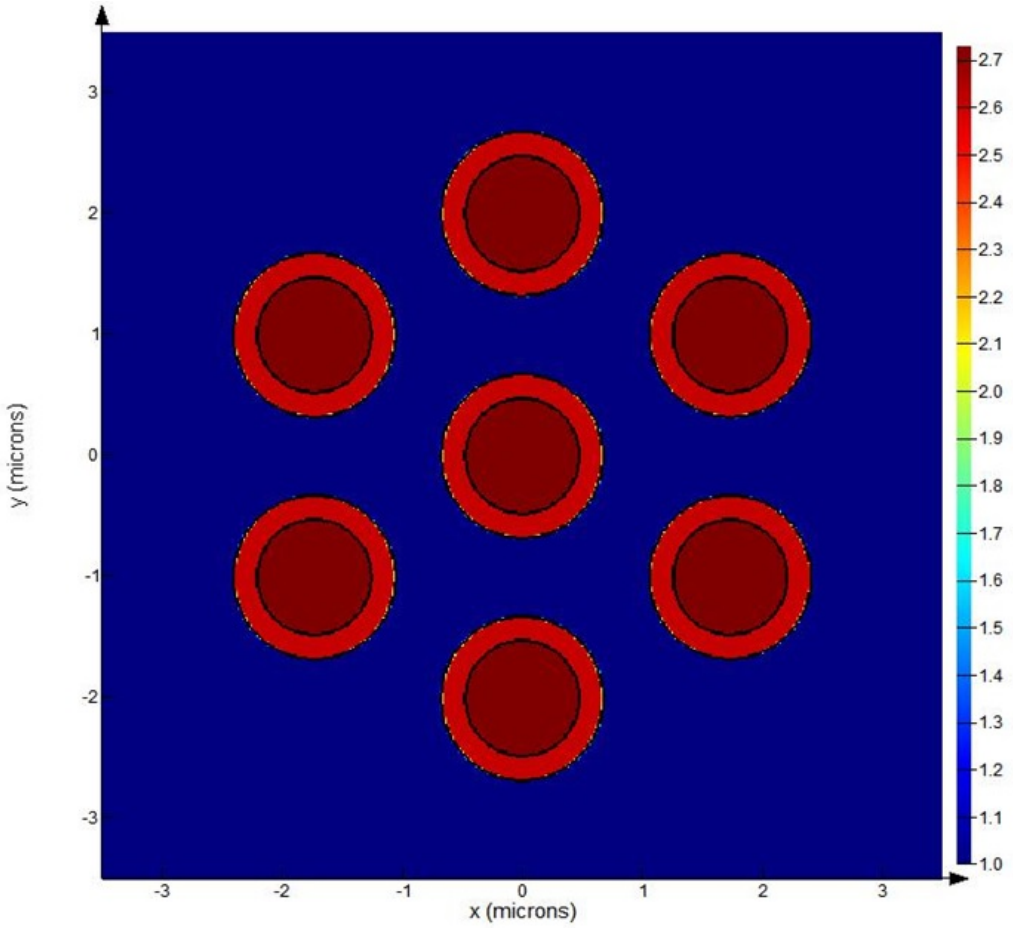

Figure 3.6: The material refractive index profile of the designed seven-core fiber calculated at 1.55 μm wavelength. $n_{core} = 2.73$, $n_{cladding}$ =2.61 and $n_{polymer}$ =1.65.

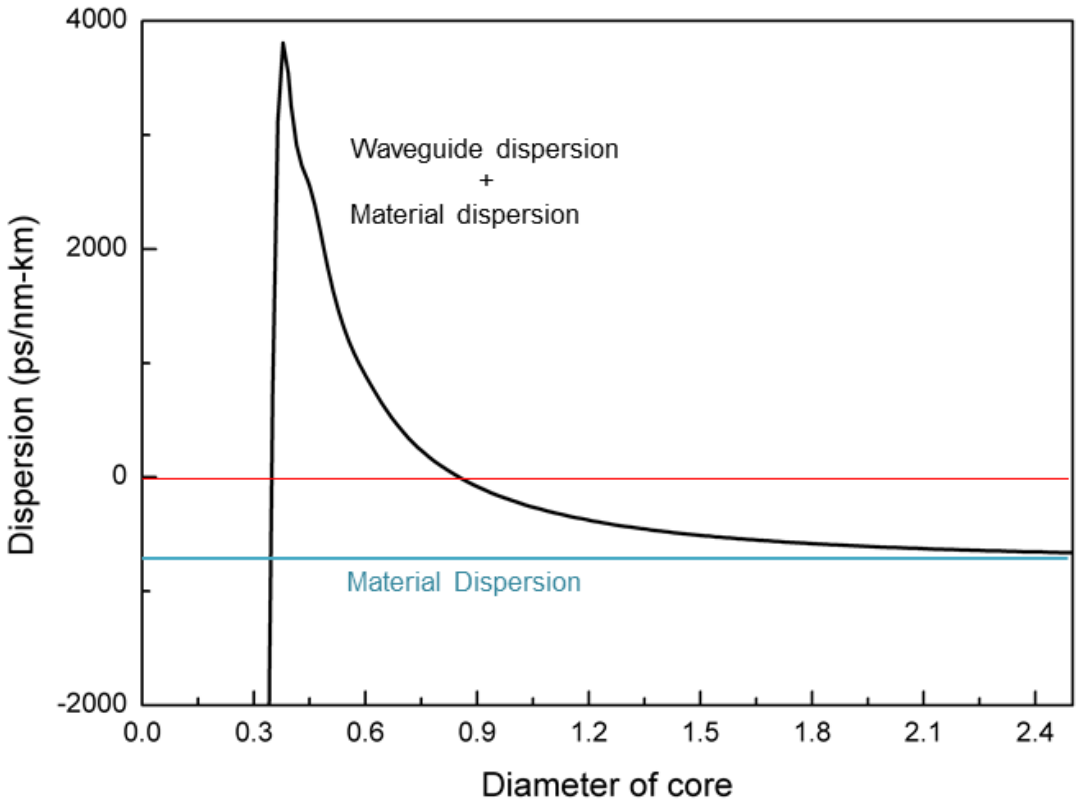

Figure 3.7: Calculated dispersion parameter of As_2Se_3 core and $Ge_{10}As_{23}Se_{67}$ cladding fiber with respect to core diameter at pump wavelength of 1.55 μm. The core diameter/cladding diameter is fixed to 0.728. The blue line shows the material dispersion of bulk core material As_2Se_3.

The ISR method ensures the preservation of the ratio at the beginning throughout the drawing process. The dispersion parameter with respect to core radius of the fiber can be deducted from Figure 3.7 and for the fiber with 0.95 μm core diameter has dispersion parameter approximately -100 ps/nm-km, this value is relatively small when we look at material dispersion of the core material, since the diameter is at the vicinity of zero dispersion. From Figure 3.7 it can be seen 1.55 μm is the ZDW for core diameter of $\sim$ 850 nm. The GVD of the fiber with 0.95 μm core diameter has β_2 =-0.128 ps^2/m which is low and acceptable for our design.

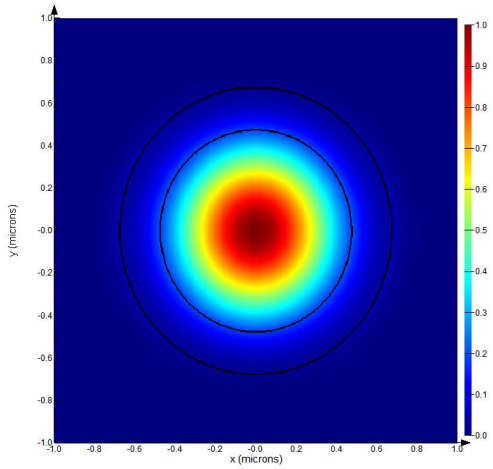

Figure 3.8: Calculated single-mode profile of the single fiber from seven-core design defined in Section 3.2. The As_2Se_3 core diameter is 0.95 μm and the $Ge_{10}As_{23}Se_{67}$ cladding radius is 1.35 μm. The black circles show the boundaries of core and cladding.

3.2.2 Single-Mode Profile

The mode profile is calculated by using Lumerical Mode Solution. The single-mode profile of a single fiber from seven-core design is shown in Figure 3.8. As_2Se_3 core diameter is 0.95 μm and the $Ge_{10}As_{23}Se_{67}$ cladding radius is 1.35 μm and their boundaries are shown with black circles.In Figure 3.8 the perfect mode coupling is seen at 1.55 μm wavelength in core of the fiber. Small amount of the light travel into the cladding with a negligible amount of leakage to the polymer jacket. In this way the absorption resulted in by polymer is decreased. The light is effectively coupled to the core which has high nonlinearity thus the interaction between nonlinear media and high intensity is provided.

3.2.3 Supercontinuum Generation Calculations

In a nonlinear medium the nonlinear Schrödinger equation (NLSE) governs the propagation of a pulse. The split step Fourier method (SSFM) is described in Section 2.x. The Generalized form of it is used to calculate the effects of nonlinearity. A Matlab code [60] is used to calculate supercontinuum evolution inside As_2Se_3 fibers. The nonlinear refractive index of As_2Se_3 is $n_2 = 2.3\times10^{-17}m^2/W$ [73]. At 1.550 μm, refractive index of As_2Se_3 is 2.73 and refractive index of $Ge_{10}As_{23}Se_{67}$ is 2.61. The numerical aperture (NA) of the fiber is 0.8. The calculations are performed for 0.95 μm core diameter, the effective area A_{eff} is calculated as 0.639 μm^2 by Equation 2.18, 2.19 and 2.20. Therefore the parameter γ is calculated as 23.2 $W^{-1}m^{-1}$, the pulse duration is 150 fs and the pump wavelength is 1.55 μm. β_2 = -0.128 ps^2 /m is determined from Figure 3.7.

The SC evolution shown in Figure 3.9 for various peak powers (a) 5 W, (b) 10 W, (c) 20W, and (d) 50 W. For 5 W, the broadening is just caused by the SPM since the power is not enough to trigger the solitonic effect. Because of very low dispersion at 1.55 μm wavelength, the temporal domain is not affected. For 10 W, the soliton fission is created after 9 cm propagation inside the fiber and a SC covers wavelength from 1 μm to 2.25 μm. For 20 W, the SC generated begins after 6 cm and spans 1-2.75 μm. For 50 W, the soliton fission occurs 3.5 cm propagation and SC is generated between 1 μm and beyond 3.5 μm. The lower boundary for broadening is 1 μm wavelength for all cases because the high dispersive property of the shorter wavelength. Light generated near to 1 μm is too dispersive and unable to create new light with shorter wavelength. The wavefront is reshaped in temporal domain by dispersion as seen in Figure 3.9(d). The fiber length can be chosen to have small change in time domain, for instance the length can be arranged to not allow propagation of light inside the fiber after the soliton fission occurs.

The calculation shows us the broadening of SC is possible from 1 μm to beyond 3.5 μm. By designing fiber with ZDW at MIR it is possible to generate more broad SC even covers entire fingerprint region like the example shown in Figure 3.1.

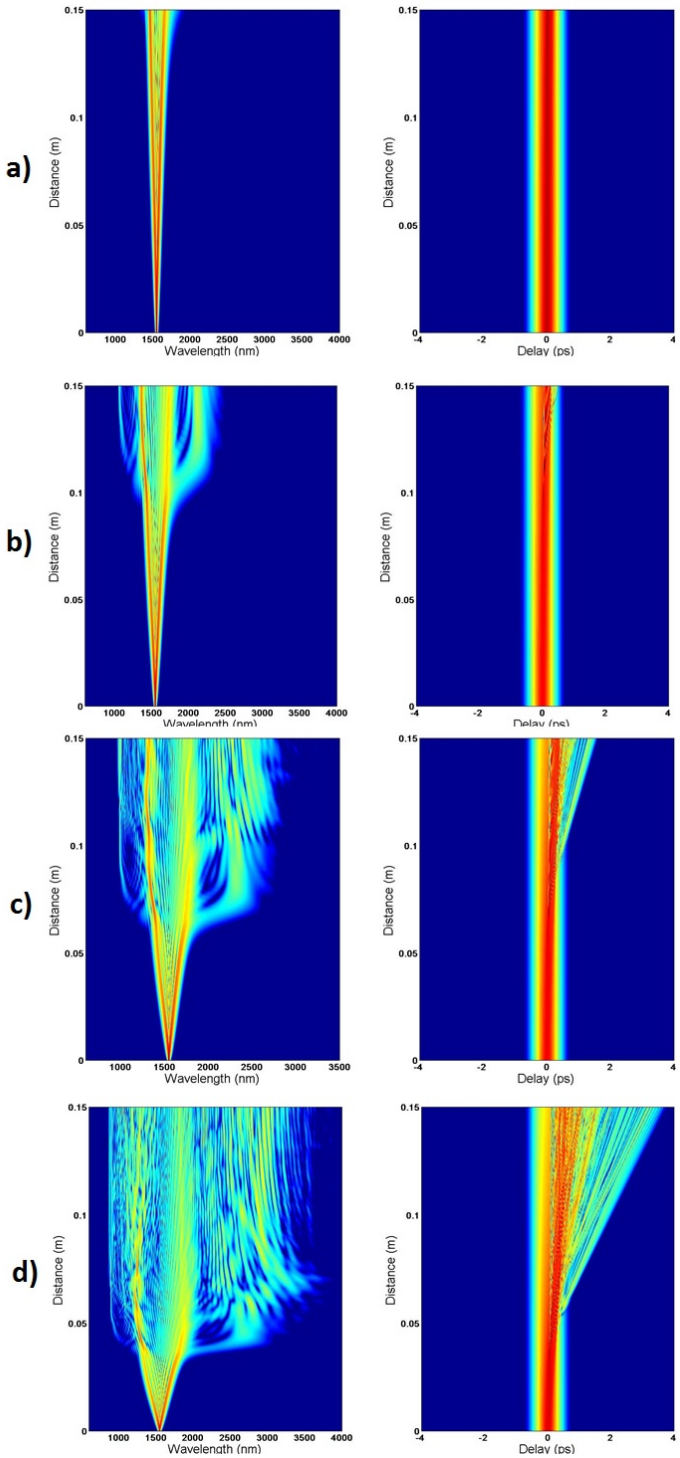

Figure 3.9: Spectral and temporal evolution of SC inside highly nonlinear 15 cm-length of single fiber with As_2Se_3 core for different peak powers (a) 5 W, (b) 10 W, (c) 20W, and (d) 50 W.

Chapter 4

Chalcogenide Glass Synthesis and Preparation of Preform

The macroscopic structure prepared for fiber drawing process is called as preform. Preform preparation is the most important part of the fiber fabrication because any failure in macroscopic preform will affect the shape and structure of the fiber in drawing process. A macroscopic preform is mostly prepared in cylindrical shape with a 20-30 mm of diameter and 100-300 mm of length. Figure 4.1 shows a preform before and after drawing process. The constituent materials of preform need to have suitable glass transition temperature since the drawing process is performed at a little beyond these temperatures.

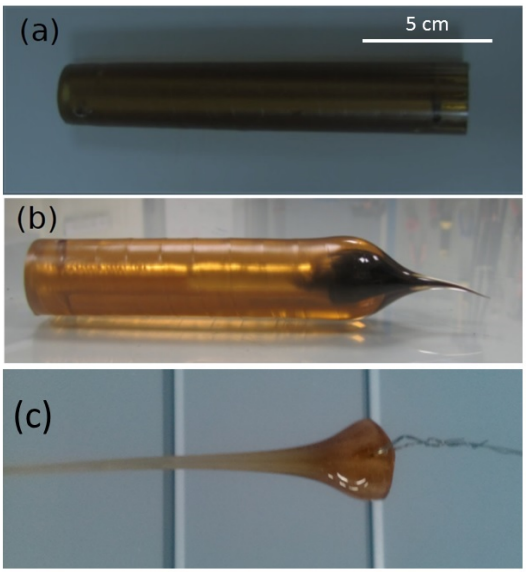

Figure 4.1: A macroscopic preform (a) before and (b) (c) after fiber drawing. (b) the remaining part after drawing process and (c) is the first coming part in fiber drawing process.

4.1 Rod-in-tube Approach for Production of Step-index Glass Preforms

Producing step-index silica preforms are standardized via modified chemical vapor deposition (MCVD). Preparation of an IR step-index preform is more challenging. The rod-in-tube approach outlined in Figure 4.2 is the most used technique to produce step-index IR preforms [5]. Figure 4.2 (a) shows the core rod fabrication via (Figure 4.2 (a-1)) melt casting; (Figure 4.2 (a-2)) thermal drawing from large bulk glass to smaller [40]; (Figure 4.2 (a-3)) extrusion [87, 88]; or (Figure 4.2 (a-4)) hot-pressing of a powder. Figure 4.2 (b) shows the production of cladding tube via (Figure 4.2 (b-1)) casting [89]; (Figure 4.2 (b-2)) drilling [68, 90]; (Figure 4.2 (b-3)) extrusion [88, 91]; (Figure 4.2 (b-4)) or rotational casting [92, 93].

There are 16 combinations of rod and tube fabrication. For rod fabrication we used melt casting and for tube preparation we used the rotational casting. In melt casting method for rod fabrication, the raw materials are batched into a

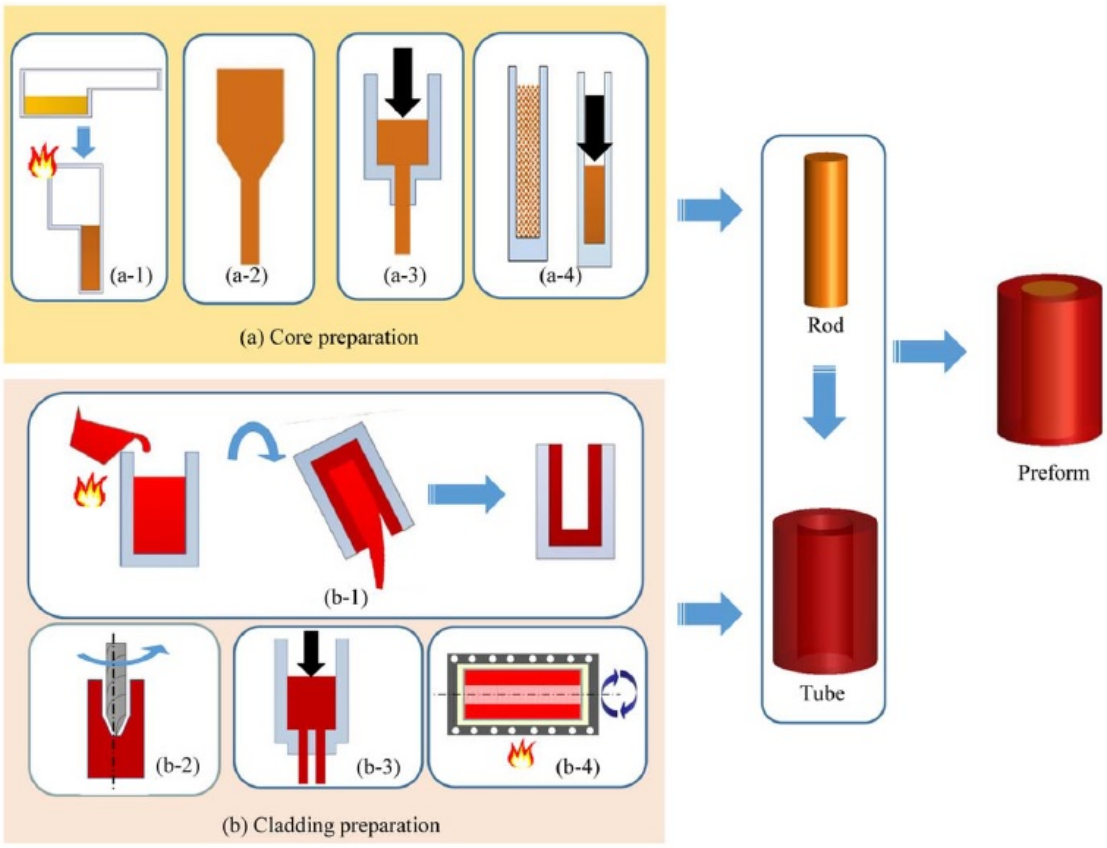

Figure 4.2: Rod-in-tube approach for fabricating IR step-index preforms (a) glass rod preparation for core of fiber via (a-1) casting; (a-2) thermal drawing; (a-3) extrusion; and (a-4) hot press. (b) Glass tube preparation for cladding via (b-1) casting; (b-2) drilling; (b-3) extrusion; or (b-4) rotational casting [5].

sealed and vacuumed container which can stand the vapour pressure of the raw materials. In rotational casting method for tube fabrication, the raw materials are batched into cylindrical container such as quartz tube mounted horizontally while the material inside the container is liquid. The mounted container is rotated with a high rotational speed until the material inside tube is cooled below the melting temperature. The applied centrifugal force by rotation provides the tube shape at the end of the process.

4.2 Preform Design

Preform is prepared in three part; core, cladding and polymer jacket. We performed the drawing process for two different combinations. As preliminary experiment, we choose $Ag_4(As_{0.4}Se_{0.6})_{96}$, $As_{40}S_{25}Se_{35}$ and polyethersulfone (PES) as core, cladding and shell respectively. Then we performed the same experiment for As_2Se_3, $Ge_{10}As_{23}Se_{67}$ and polyetherimide (PEI) as core, cladding and shell respectively. The core materials were chosen since they are the best-known highly nonlinear chalcogenide glasses and we tried to raise the nonlinear index of the core material. Table 2.1 shows $Ag_4(As_{0.4}Se_{0.6})_{96}$ has 2190 times and As_2Se_3 has 833 times higher nonlinear refractive index than fused silica. The cladding materials are chosen to provide the step index structure of fibers and their low loss in MIR region. Also they are chosen to engineering the NA of the fiber as high as possible. This will be detailed later in this chapter. To obtain the preform shown in Figure 4.3, we fabricated chalcogenide glass rod, chalcogenide glass tube that has an inner diameter similar to the rod and polymer jacket whose inner diameter is chosen equal to the outer diameter of glass tube. The chalcogenide glasses were fabricated with melt-quenching method, the tubes are obtained by rotational casting and the polymer jackets were produced by thin film polymer rolling followed by consolidation. This will be detailed later in this chapter.

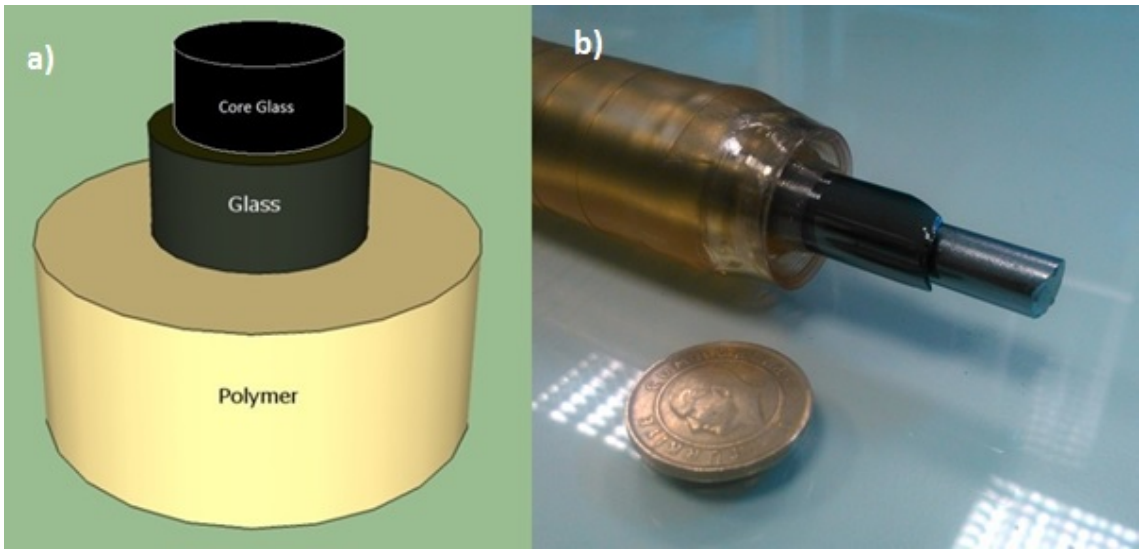

Figure 4.3: The design of our preform (a) schematic representation (b) after producing all components of the preform.

4.3 Preparation of Rod and Tube Chalcogenide Glasses

Bulk chalcogenide glasses in this study were prepared using conventional melt-quenching method. Before chemical vapor deposition and sol-gel technique, melt quenching was the only method used to fabricate chalcogenide glasses [94, 95]. Melt-quenching method provides to produce large amount of materials compared to the others with high flexibility in geometry and variety of materials that can be produced using this method. This method also provides of flexibility of doping glasses with active ions or metals.

The melting process must be performed in the environment purified from oxygen and water to obtain high-purity glasses. The melting of ChGs must be carried out in evacuated and sealed quartz tube to preserve the high impurities of materials. Here, we used As, Se, Ge, and Ag, which are stored in a glovebox shown in Figure 4.4 as raw materials with 99.999 purity and prefabricated As_2Se_3 was used to produce the $As_{40}S_{25}Se_{35}$ tube for preliminary experiment. After melting

Figure 4.4: The glovebox used in batching chemicals to quartz ampoules.

the raw materials filled into quartz ampoules, the melt needs to be shaken to provide mixing and homogeneity. A rocking furnace has an important role in melting process to shake the melt and promote the raw elements react to form a ChG liquid.

Table 4.1: The raw material materials weighed and poured to quartz tube with given ID (inner diameter) and OD (outer diameter).

Material	$As_{(g)}$	$Se_{(g)}$	$As_2S_{3(g)}$	$Ag_{(g)}$	$Ge_{(g)}$	$Total_{(g)}$	$ID/OD_{(mm)}$
$As_{40}S_{25}Se_{35}$	5.23	8.42	6.43			20	10/15
$Ge_{10}As_{23}Se_{67}$	5.57	17.1			2.39	25	10/15
As_2Se_3	9.68	15.32				25	8/10
$Ag_4(As_{0.4}Se_{0.6})_{96}$	9.17	14.5		1.377		25	8/10

4.3.1 Batch Chemicals

Two different sizes of quartz tubes used to process melting. The tubes used for tube production had inner diameter (ID) of 10 mm and outer diameter (OD) of 15 mm, and the other tubes for rod production had ID of 8 mm and OD of 10 mm. All of the quartz tubes were cleaned with acetone and distilled water several times, then their open ends were covered with aluminum folio. After cleaning, the tubes were dried into vacuum cell at 110 ℃ at least 1 day to get rid of the adherent liquid residuals at inner surface. The tubes and a Saunders valve were inserted into a glovebox as in the Figure 4.4, circulated with nitrogen with reduced oxygen and water ($\leq$ 0.1 ppm). After deciding the molecular formulas of the glasses need to be produced, the required masses of each raw material were calculated. The materials were weighed carefully according to Table 4.1 inside the glove box and poured into the tubes. The tubes are connected from their open end one by one to a Saunders valve to prevent any leakage inside the tubes and extracted from the glovebox.

4.3.2 Vacuuming and Sealing

After the tubes were taken out of the glovebox they were connected to vacuum system. The system shown in Figure 4.5 consists a mechanical pump, a turbo pump, a cold trap, the Sanders valve and tubes. Those were attached to each by connection pipes resistive to high vacuum. Here, we used elements which are hazardous for health. Therefore, we attached a cold trap to system and filled the trap with liquid nitrogen to decrease the flow of evaporated elements, especially sulfur and selenium. The connection pipes were evacuated and filled with gaseous nitrogen to clean out the oxygen from the pipes before opening the valve. Then, the evacuation was conducted again and the valve opened to evacuate the tubes, the tubes were purged with nitrogen 2 or 3 times and evacuated 10^3 mBar. Then the elements in the tubes were air-baked with oxygen-natural gas flame for 1 minute to get rid of the residual liquids and oxygen inside the quartz tube surface. Then the tubes were sealed by using oxygen-natural gas flame, the

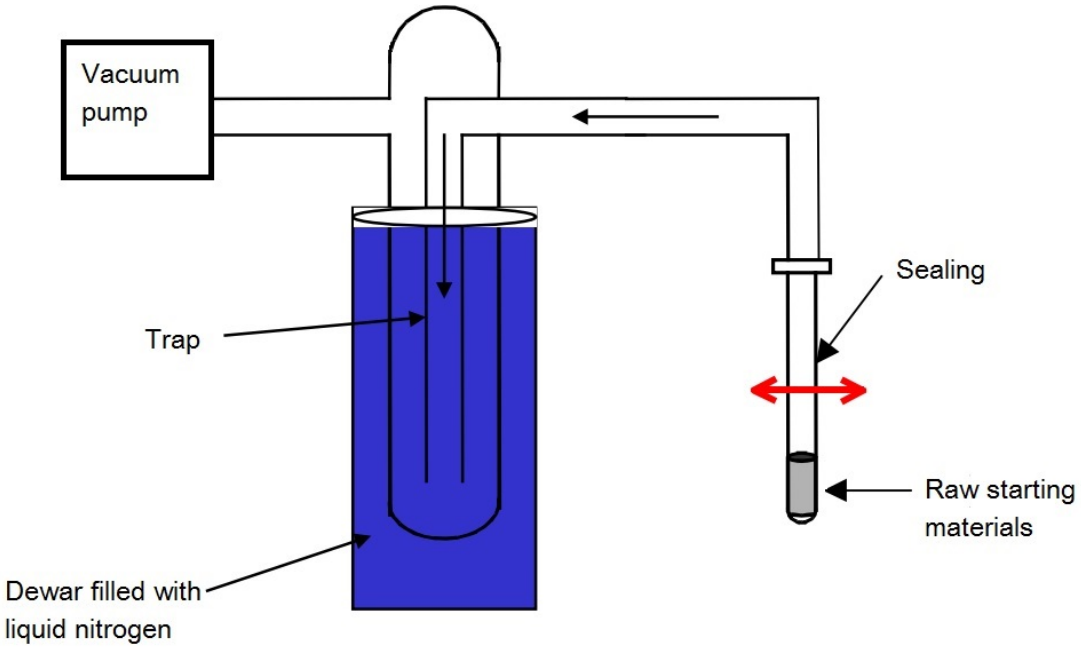

Figure 4.5: Typical vacuuming and sealing setup used for fabrication of ChGs in sealed quartz ampoule.

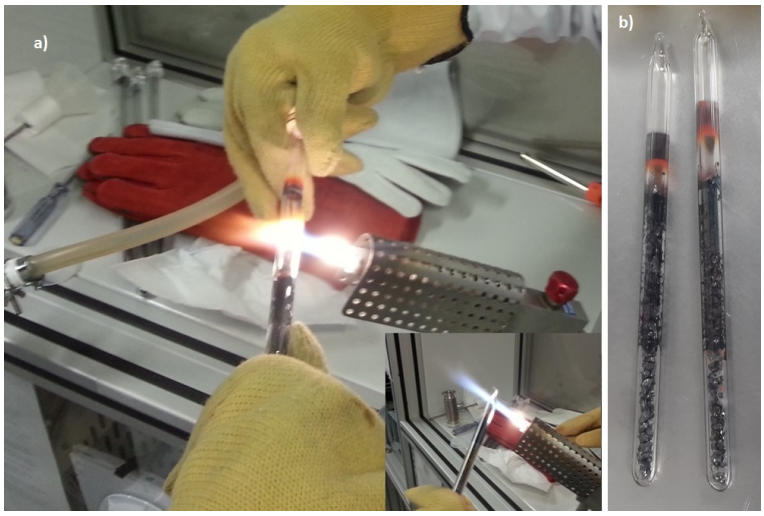

Figure 4.6: (a) Sealing of evacuated tubes under high vacuum. (b) The sealed tubes with the raw materials.

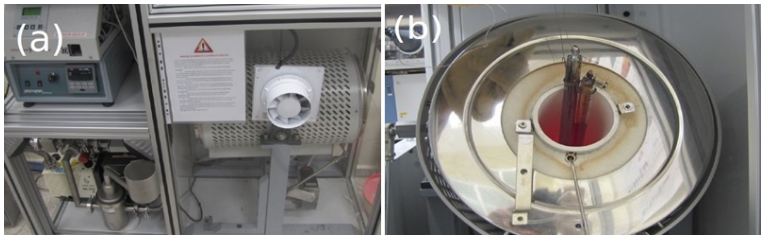

Figure 4.7: (a) rocking furnace used in melt process. (b) The melted ChG inside the evacuated quartz tube.

sealing process and the resultant tubes with raw materials are shown in Figure 4.6. We used just $As_{40}S_{25}Se_{35}$ and $Ge_{10}As_{23}Se_{67}$ to fabricate ChG tube. The lengths of the quartz tubes after sealing were pre-calculated to obtain desired inner diameter. The sealed quartz tube lengths were 15 cm for $As_{40}S_{25}Se_{35}$ and 18 cm for $Ge_{10}As_{23}Se_{67}$.

Table 4.2: The rocking furnace temperatures for different materials.

Material	Rocking furnace temperature
$As_{40}S_{25}Se_{35}$	700
$Ge_{10}As_{23}Se_{67}$	850
As_2Se_3	700
$Ag_4(As_{0.4}Se_{0.6})_{96}$	1000

4.3.3 Melting, Quenching and Rotational Casting

The evacuated tubes inserted to a rocking furnace shown in Figure 4.7 in different times since their operational temperature is different. For instance, the melting process of raw materials including sulfur is need to be operated in lower temperature than others because of high vapor pressure of the sulphur. The tubes were tied with wires resistant to high temperatures to make the extraction of them easy and wrapped into thermal blanket to protect the tubes and heat them homogenously. As common we increased the furnace temperature to 400 ℃ by the increment of 15 ℃ per minute and waited here at least 1 hour. Then the temperature was increased by the increment of 2 ℃ per minute up to the desired temperature, which is different for different materials as shown in Table 4.2

The rocking furnace had a rocking angle 30-40° above and below horizontal axis. The rocking furnace was rocked when the temperature reached the desired point. The rocking process needs to be operated for several hours to provide complete homogeneity of the materials. Here, the tubes rocked for 2-4 hours and total melting procedure lasted for approximately for 18-24 hours.

The rocking furnace was held vertical position as possible as seen in Figure 4.7 (b) before quenching. Quenching can be carried out in water or air. The glasses for solid rod were quenched in water as seen in Figure 4.8 (b). The glasses for tube fabrication were quenched in air while rotating in a rotator machine in Figure 4.9. The hand-made rotator machine rotates a high-temperature resistant ceramic tube with ID of 15 mm around the horizontal axis. The tubes filled with melted liquids of $As_{40}S_{25}Se_{35}$ and $Ge_{10}As_{23}Se_{67}$ were placed into the ceramic

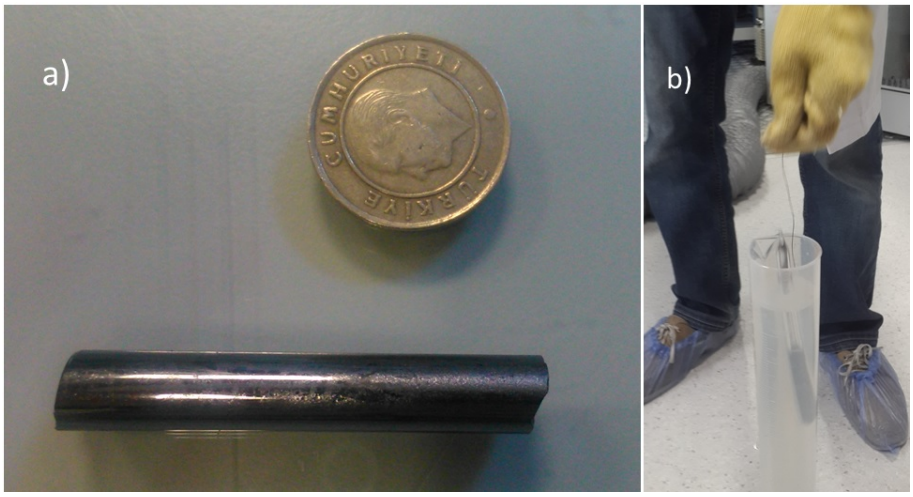

Figure 4.8: (a) The fabricated As_2Se_3 rod. (b) The quenching of the melted ChG in water.

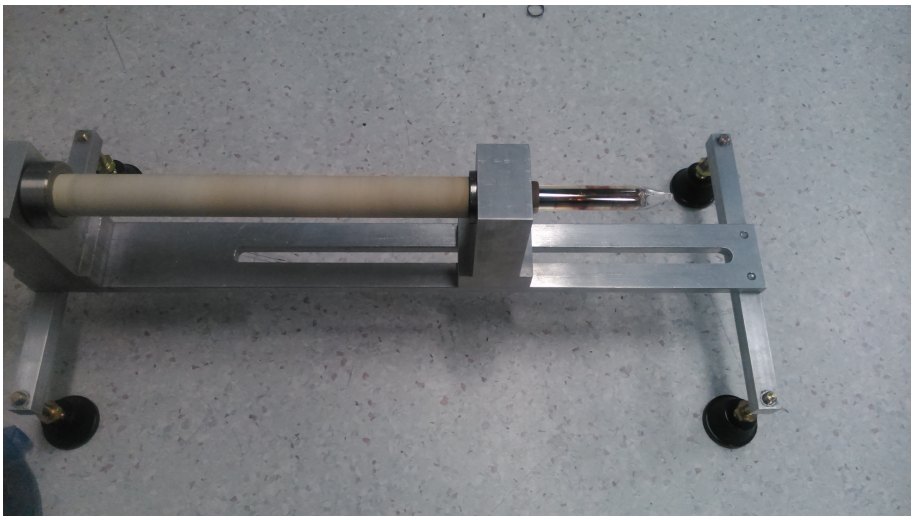

Figure 4.9: The quartz tube with melted ChG installed and rotated by the rotator machine used for rotational casting

Figure 4.10: The $Ge_{10}As_{23}Se_{67}$ tube fabricated by rotational casting

tube of rotator machine in a few seconds after extracted from the rocking furnace and rotated with high speed.

After cooling the materials inside the sealed tubes were extracted by breaking the quartz tubes. As_2Se_3 rod in Figure 4.8 (a) with 8 mm is fabricated and $Ge_{10}As_{23}Se_{67}$ tube in Figure 4.10 with inner ID of 7.8 mm and OD of 10.3 mm was fabricated. The As_2Se_3 was polished to obtain the same diameter with the ID of the $Ge_{10}As_{23}Se_{67}$ tube.

4.3.4 Optical Characterization

The ellipsometric measurements were conducted by J.A. Woollam Vis-NIR Ellipsometer System. ChGs were coated on silicon wafer pieces already cleaned from dust and other particles by the help of a thermal evaporator. We coated the ChGs synthesized from 10 to 50 nm thicknesses since the thickness of ChGs in between 10 nm and 50 nm is suitable for ellipsometric measurement. The thickness higher than 50 nm can be suitable with suitable fitting method. We used Tauc-Lorentz

model fitting for all ChGs as defined in a previous study about how to analyze a spectrometric ellipsometry data of ChGs [96].

The refractive indices of $Ag_4(As_{0.4}Se_{0.6})_{96}$ and $As_{40}S_{25}Se_{35}$ and the numerical aperture (NA) of the fiber consists of these materials as core and cladding respectively are shown in Figure 4.11. The NA of a fiber can be calculated by the relation given by

$$NA = \sqrt{n_{core}^2 - n_{cladding}^2} \tag{4.1}$$

Note that the NA for an optical fiber does not determine the acceptance angle of the fiber. The NA becomes only an approximation especially for SMF. The acceptance angle for SMF is different and refraction indices are not the only determinant.

The refractive indices of these two materials at 1550 nm are 2.8 and 2.63; thredore, the NA is 0.96 at this wavelength. The refractive indices of As_2Se_3, $Ge_{10}As_{23}Se_{67}$, and the NA of the fiber will consists these materials as core and cladding respectively are shown in Figure 4.12. The refractive indices of these two materials at 1550 nm are 2.73 and 2.61; as a result the NA is 0.8 at this wavelength. NA can be engineered using different materials for cladding.

The extinction coefficients were also calculated simultaneously. Figure 4.13 shows the extinction coefficients of all four ChGs fabricated in this study. The absorption edge for 4% Ag doped As_2Se_3 (stated as $Ag_4(As_{0.4}Se_{0.6})_{96}$) shifted from 690 nm to 900 nm. As seen in the figure the ChGs have no absorption related to the extinction coefficients for longer wavelengths than 900 nm, which is vital for IR applications. As_2Se_3 and $Ge_{10}As_{23}Se_{67}$ which were used for the fiber drawn and shown in Chapter 5 have no absorption for longer wavelengths than 690 nm.

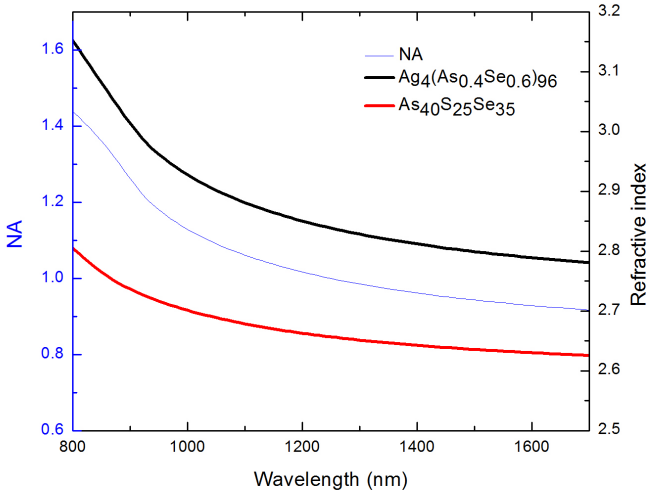

Figure 4.11: The refractive indices of $Ag_4(As_{0.4}Se_{0.6})_{96}$ and $As_{40}S_{25}Se_{35}$ and the NA of the fiber will consists these materials as core and cladding respectively.

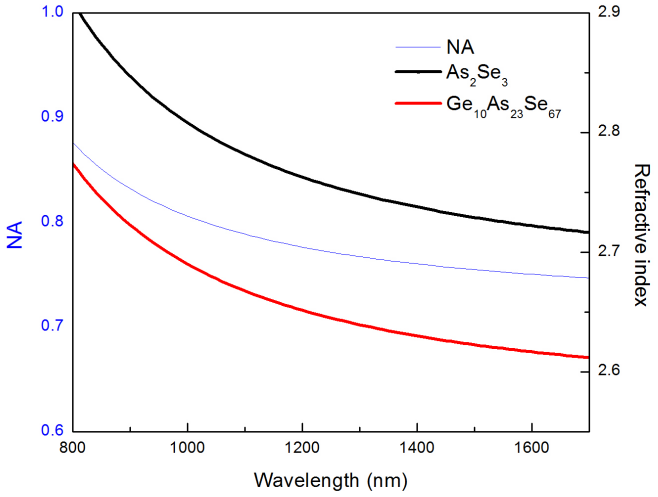

Figure 4.12: The refractive indices of As_2Se_3, $Ge_{10}As_{23}Se_{67}$, and the NA of the fiber will consists these materials as core and cladding respectively.

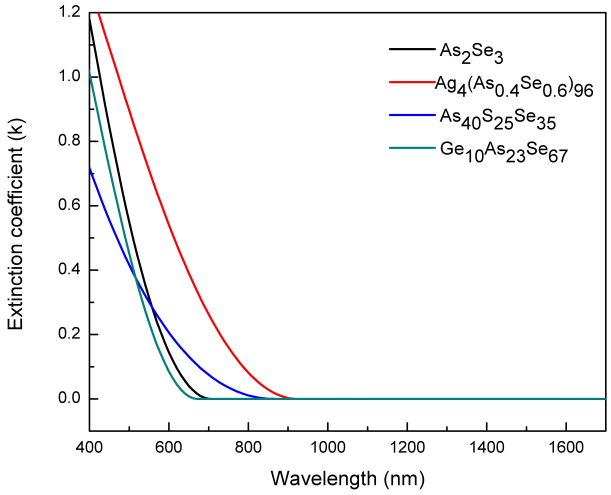

Figure 4.13: Extinction coefficients of the ChGs synthesized

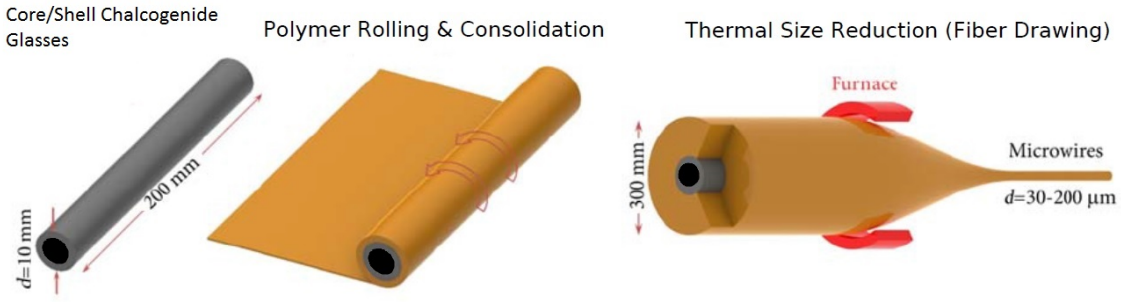

Figure 4.14: A model that shows polymer rolling, consolidation and fiber drawing processes.

4.4 Polymer Jacket Preparation

Polymer jacket production is an important part of preform preparation. Any failure in the macroscopic scale polymer rod affects the fiber drawing process. Therefore, everything needs to be conducted in a proper way to eliminate the possible failures. A unique process to fabricate a polymer rod with a hole is through rolling thin polymer film rolling and consolidating it under vacuum. A schematic representation of polymer rolling and consolidation is shown in Figure 4.14. The polymer rod needs to be fabricated as the glass rod and tube fits into it. We fabricated polymer rods for each fiber drawing step to solidify the resultant fiber at each steps.

4.4.1 Thin Polymer Film Rolling

We fabricated polymer rod from two different materials. For preliminary test the polymer rod was fabricated from PES and for the other experiment we fabricated PEI polymer rod. The polymer film rolling process is shown in Figure 4.15 . The polymer film was first cut with 15 cm width. As in Figure 4.15(a), the polymer film was cleaned by the help of alcohol and cleanroom fabric, and then the cleaned thin film was placed to a vacuucell with temperature of 110 ℃ one night before rolling to get rid of residual water. A glass rod was chosen with the same OD or slightly higher OD of ChG tube manufactured. A thin teflon sheet was rolled to the glass rod to avoid the polymer stick to the glass rod while consolidation process. The polymer film was rolled as shown in Figure 4.15 (b) by hand tightly around the glass rod until it reaches to the intended total diameter; we chose the polymer rod diameter of 25-28 mm for all steps. The last layer of the polymer film was stuck with vacuum tape as seen in Figure 4.15 (c) and the rolled polymer thin film was covered with teflon tape as seen in Figure 4.15 (d) to avoid dirt and keep the polymer together while consolidating.

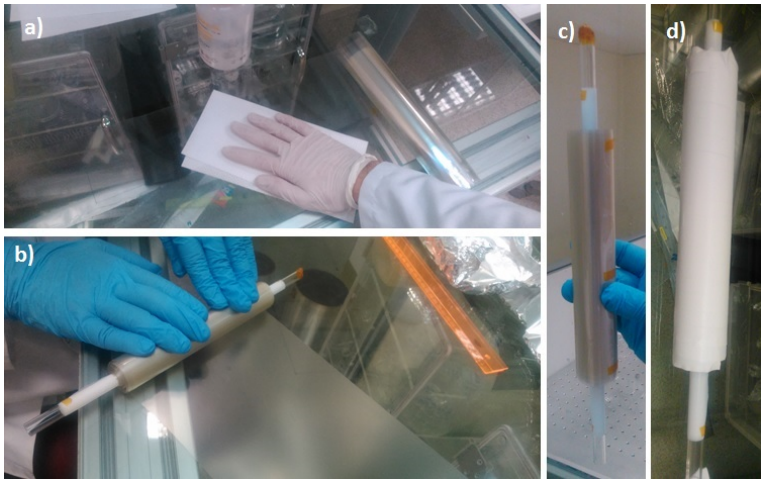

Figure 4.15: Preparation of the polymer jacket for consolidation.

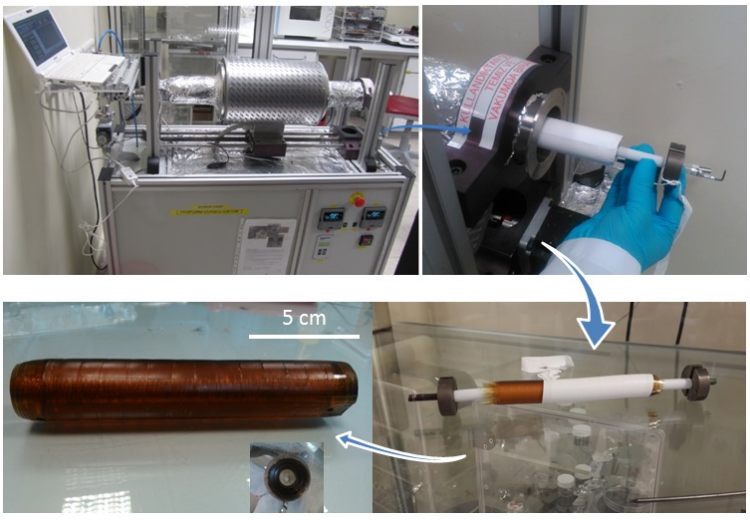

Figure 4.16: Consolidation of polymer in an evacuated consolidation furnace.

4.4.2 Consolidation

The prepared polymer preform was located at the middle of the consolidation furnace shown in Figure 4.16. The heating process was programmed by using a computer. The furnace was first programmed to 180 ℃ with the increment of 15 ℃ per minute and kept at that temperature for 3 hours to get rid of the liquid or gaseous residuals between the layers of rolled thin film. Then the furnace was heated with the increment of 2 ℃ to 240 ℃ for PES and 253 for PEI, the consolidation conducted in these temperatures for 20 and 35 minutes, respectively. Then the furnace was opened without waiting for cooling and the polymer preform extracted to cool down at room temperature. The glass rod and teflon tape were removed after cooling. At the end, the intended polymer preforms were prepared as in Figure 4.16.

Chapter 5

Fabrication of Multicore Fiber

Optical fibers are commonly fabricated by thermally drawing of a macroscopic preform. The preform is held vertically and fed into a preform furnace that heats and softens the preform, and an external force pulls the softened material downward, for polymer preform, generally, drawing a mass (50-200 g) is hanged to material to provide the external force. The preform stretches into a thin fiber by the help of the hanged mass. Then the fiber is attached to a capstan to pull the fiber with a constant force and speed. Thermal drawing enables fabrication of thousands of kilometers-long uniform optical fibers.

In this study, fiber drawing was carried out using house-made fiber drawing tower shown in Figure 5.1. The fiber tower is 2.5 meters in height and consists of a downfeed, a holder with X-Y stage, a preform furnace, a diameter sensor, a tension measurement tool and a capstan. The thermally drawing of a single material is related to the glass transition temperature. The drawing of chalcogenide glasses to micrometers requires typically a polymer jacket to solidify the glass core. The multimaterial fiber drawing needs to be performed in the temperature region in between glass transition (T_g) and melting temperatures (T_m) of the constituent materials if there is no crystallization or oxidation of them in this region. If there is a crystallization region for materials the drawing needs to be conducted more carefully. A typical differential scanning calorimetry (DSC)

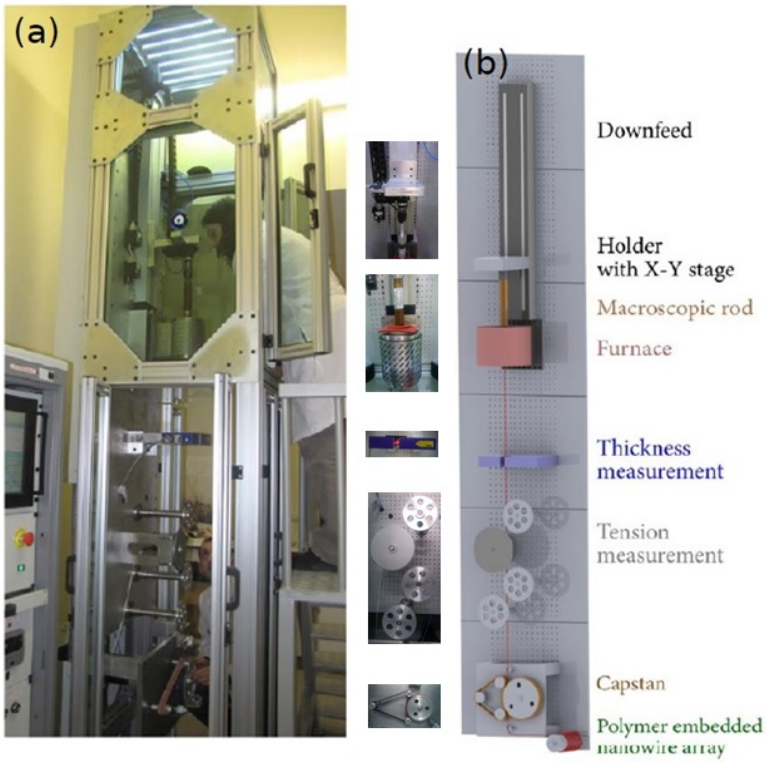

Figure 5.1: (a) Fiber tower used in this study. (b) The components of the fiber tower are shown schematically.

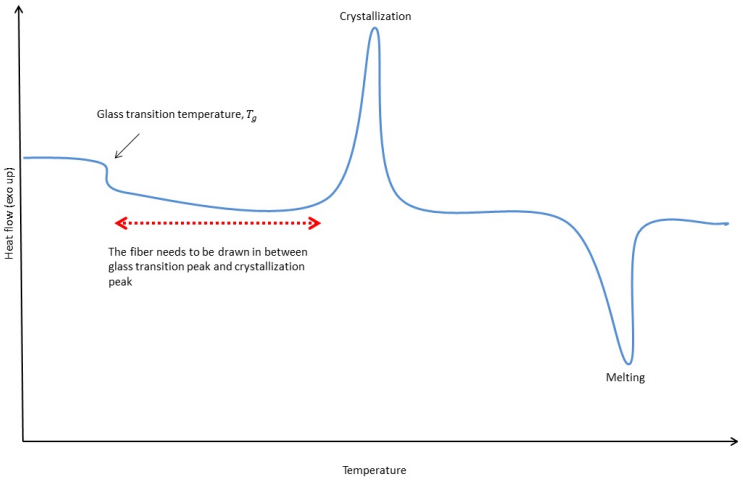

Figure 5.2: Typical DSC curve

thermogram shows the T_g, T_m and crystallization temperature of a material, a good example is shown in Figure 5.2. The thermogram may include the cross linking and the oxidation temperatures. Figure 5.3 shows DSC measurements for As_2Se_3, PES, and PEI. The T_g of As_2Se_3, PES, and PEI are approximately 180, 220 and 220 ℃ respectively. The thermal drawing of these materials can be conducted beyond these temperatures.

5.1 The Iterative Size Reduction Method

Yaman et al. [70] showed a new iterative size-reduction method (ISR) in 2011. This method provides fabrication of indefinitely long nanowire arrays in a flexible polymer fibre matrix from starting a multimaterial macroscopic rod. In the ISR method, multimaterial rod is reduced to arrays of nanowires in a few steps. The fibers obtained from previous step are used as raw material of the next step. A model of the ISR method is shown in Figure 5.4 . By this method it is possible to produce indefinitely long polymer embedded arrays of nanowires.

This method is used to produce the seven-core-structure defined in Section

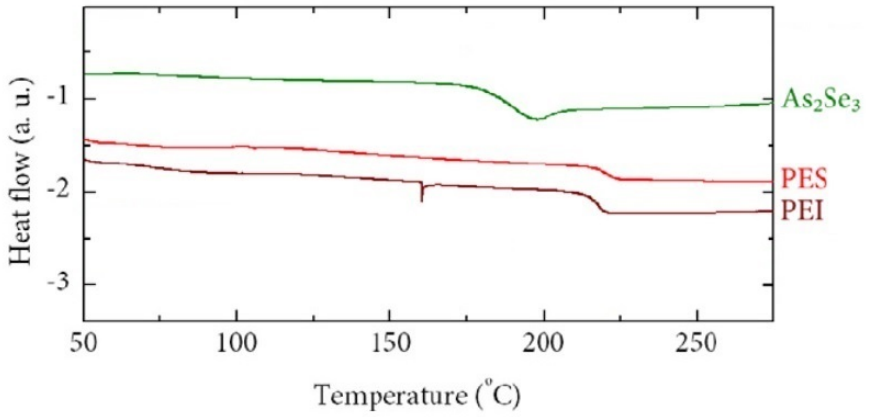

Figure 5.3: The DSC measurements of As_2Se_3, PES, and PEI.

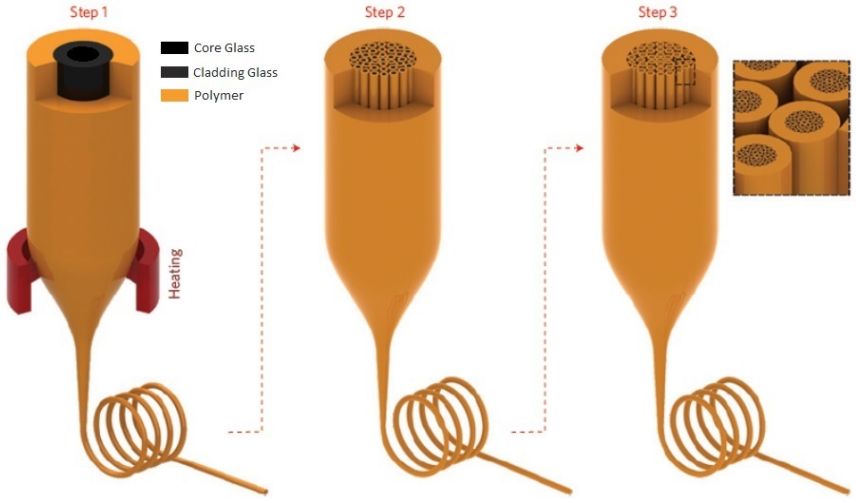

Figure 5.4: A schematic shows the iterative size reduction method.

3.2. Our seven-core design is achievable with this method since high precision hexagonal packing of As_2Se_3 is achieved [70]. This method provides us to control the diameter of the ChGs fiber.

5.2 Preliminary Test

The most decisive feature of materials is the nonlinear refractive index for SC generation. In Table 2.1, $Ag_4(As_{0.4}Se_{0.6})_{96}$ has the highest nonlinear refractive index, its nonlinear refractive index is 2190 times higher than fused silica. Therefore, as preliminary experiment we tried to draw fiber in our seven-core design. The $Ag_4(As_{0.4}Se_{0.6})_{96}$ rod, $As_{40}S_{25}Se_{35}$ and PES polymer tube were manufactured for this purpose. The rod was intentionally placed to 2 cm above of the tip of the preform; we intended to stabilize the fiber drawing by just drawing the polymer tube before drawing the glasses. The drawing started at 310 ℃ and the temperature was reduced to 295 ℃ just after the drawing began. The feeding speed was fixed to 12 mm/min and the capstan speed was 0.3 rpm.

The preliminary test was failed, when the drawing reached to $Ag_4(As_{0.4}Se_{0.6})_{96}$ rod the rod broke to pieces in polymer jacket as seen in Figure 5.5 (a). Figure 5.5 (b) shows the change on the core material after drawing, the material before drawing was glossy (right) and after drawing it became matte (left). The change in glossiness shows us the phase change of the material during drawing process. Figure 5.6 shows the DSC data of $Ag_4(As_{0.4}Se_{0.6})_{96}$, the T_g of the material is approximately 170 ℃. There are two other peaks which are crystallization and oxidation peaks having highest points at 230 and 280 ℃ respectively. The crystallization of material begins at 220 ℃. Also the powder X-ray diffraction (XRD) measurement of the $Ag_4(As_{0.4}Se_{0.6})_{96}$ in Figure 5.7 shows the phase change. The red curve is powder XRD measurement of the material before the drawing, the smoothness of the curve implies the material is in amorphous state before drawing. The black curve is the powder XRD measurement of the material after thermal drawing, the sharp peaks in graph proves the phase change from amorphous to crystal during the thermal process. The material may be suitable

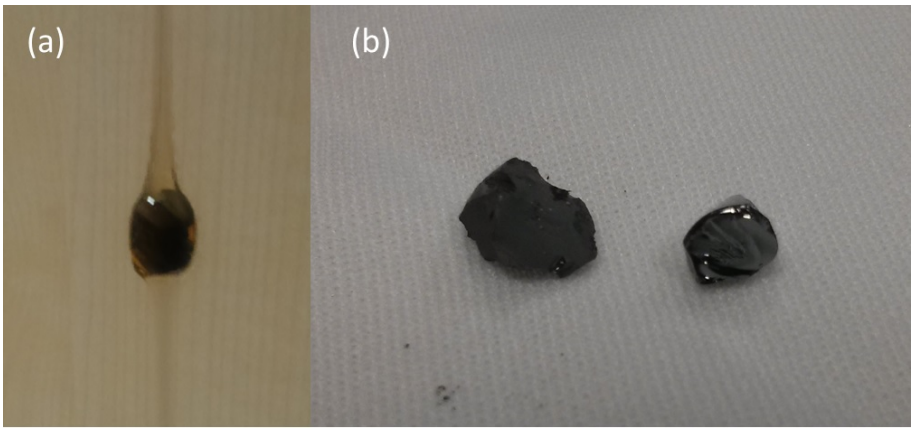

Figure 5.5: The preliminary attempt of fiber drawing. (a) The materials inside the polymer did not soften and broke to pieces. (b) The photo of the $Ag_4(As_{0.4}Se_{0.6})_{96}$ before (right, shiny) and after (left, matte) drawing.

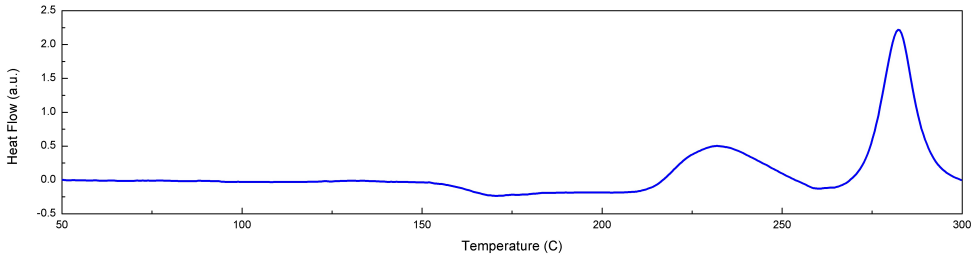

Figure 5.6: The DSC data of $Ag_4(As_{0.4}Se_{0.6})_{96}$.

for drawing with different polymer if there any suitable at temperature between the T_g and the point when crystallization begins. However, $Ag_4(As_{0.4}Se_{0.6})_{96}$ is not suitable with PES and PEI we used since they have T_g at 220 ℃ where the crystallization of $Ag_4(As_{0.4}Se_{0.6})_{96}$ begins.

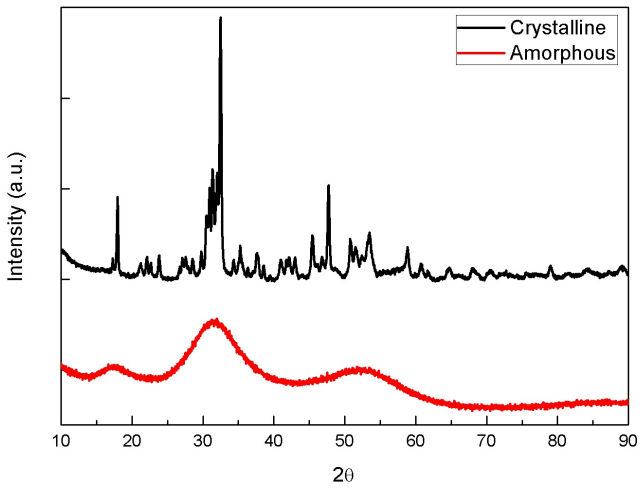

Figure 5.7: The powder X-ray diffraction measurement of the $Ag_4(As_{0.4}Se_{0.6})_{96}$ drawn as preliminary test before (red) and after (black) the fiber drawing. The measurements show the material crystallized during the drawing process.

5.3 Results and Discussion

The preliminary test showed us the fabrication of $Ag_4(As_{0.4}Se_{0.6})_{96}$ fiber is not available with PES and PEI. Therefore, we changed the core material to As_2Se_3 which has 833 times higher refractive index than silica. We decided to change the cladding material to $Ge_{10}As_{23}Se_{67}$ to eliminate the risks that may be possibly leaded by the vapor pressure of sulphur element in $As_{40}S_{25}Se_{35}$. Generally, PES preforms drawing starts around 310 ℃ and PEI preforms drawing starts around 330 ℃. As polymer jacket we decided to conduct our experiment with PEI jacket for this time to raise the operation temperature. The T_g of As_2Se_3 and PEI are 180 ℃ and 220 ℃ respectively as seen in Figure 5.3. The T_g of $Ge_{10}As_{23}Se_{67}$ is around 180 ℃. These materials are suitable for multimaterial drawing.

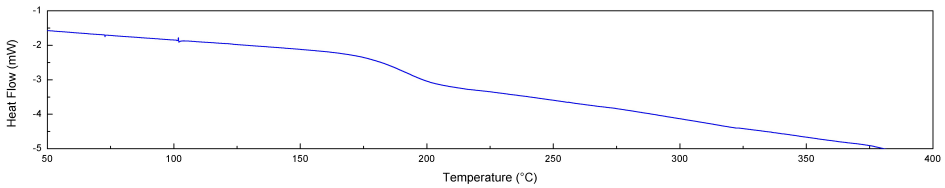

Figure 5.8: The DSC data of $Ge_{10}As_{23}Se_{67}$. The T_g is at approximately 180 ℃.

Figure 5.9: The preform was prepared for the first step drawing.

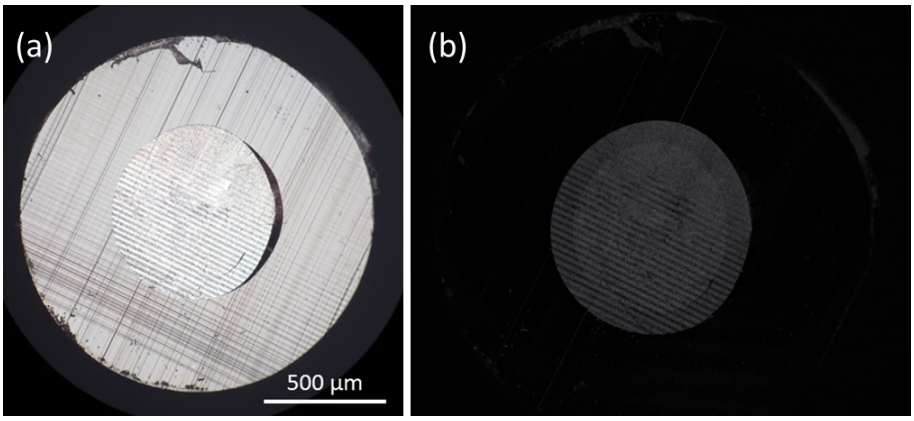

Figure 5.10: The optical microscopy images of cross-section of first step fiber (a) bright field, (b) dark field. The boundaries of cladding and polymer are obvious in the bright field image but it is not possible to distinguish the core. The boundary of between core and cladding becomes distinguishable in dark field image.

5.3.1 First Step Drawing

The core material (As_2Se_3 rod), cladding material ($Ge_{10}As_{23}Se_{67}$) and polymer jacket (PEI tube) were placed like Figure 5.9. The total diameter of the preform was 26.5 mm. The ends of the polymer tube were sealed with PEI to fix the ChGs inside the polymer tube and the preform hanged to fiber drawing tower in Figure 5.1. The preform was lowered until the section of preform, where we desired to start the first tapering, enters into the preform furnace. The furnace was programmed first to 330 ℃ and the drawing started 15 minutes after the temperature reached that point. After drawing began, temperature was reduced to 305 ℃, the hanged mass was removed and the fiber was attached to the capstan. The capstan speed was 0.2 rpm, the feeding speed was 11 mm/min. The fiber diameter was fixed to 1.6 mm for first step drawing. The reduction factor can be calculated as

$$\textit{The reduction factor} = \frac{\textit{Preform diameter}}{\textit{Diameter of Resultant fiber}} \tag{5.1}$$

The reduction factor for first step was 16.56. This implies the diameter of the cladding material will be reduced 16.56 times from 10 mm to around 600 μm. The bright and dark field images of first step fiber in Figure 5.10 shows the

diameter is very close to the calculated diameter.

5.3.2 Second Step Drawing

In second step drawing, the fiber fabricated in first step was used. The fiber was cut to 10 cm-long fiber pieces. A PEI tube was fabricated with ID of 8 mm and OD of 26 mm. Seven first-step fibers were placed in hexagonal geometry (one in middle and other six around the fiber in the middle) into the middle of the polymer tube to obtain the seven-core-structure. The space between the structure and the inner wall of the polymer tube was filled by single material PEI fibers and the seven-core-structure was compacted in this way. This compaction preserved the structure throughout the drawing process. The drawing process was similar with the first step drawing. This time we fixed the fiber diameter to 1.5 mm, the capstan speed was 0.25 rpm and the reduction factor was 17,33. We calculated to obtain ChGs fiber to have total diameter of 35 μm. The cross-sectional scanning electron microscopy (SEM) image is shown in Figure 5.11. The ChGs fibers embedded in polymer seems does not preserve their circular shape but this part is from the beginning of the drawing before stabilization of the drawing. Figure 5.13, Figure 5.14 and Figure 5.15 show that the circular shape of the ChGs were well-preserved during second and third step drawing. Figure 5.11 shows us the seven-core-structure was achieved after second step drawing.

5.3.3 Third Step Drawing

Fiber drawn in second step was cut into 15 cm-long pieces, 34 of them were stacked into PEI tube with ID of 8 mm and OD of 26 mm as seen in Figure 5.12. The same drawing procedure was conducted. In third step, the temperature was decreased to 315 ℃ rather than 305 ℃ and the capstan speed was raised to 0.5 rpm. The feeding speed was same with the first two steps. The changes in parameters were done to fix the diameter of fiber to 1 μm and the reduction factor to 26. In this way we can reduce the total diameter of ChGs fiber in polymer to

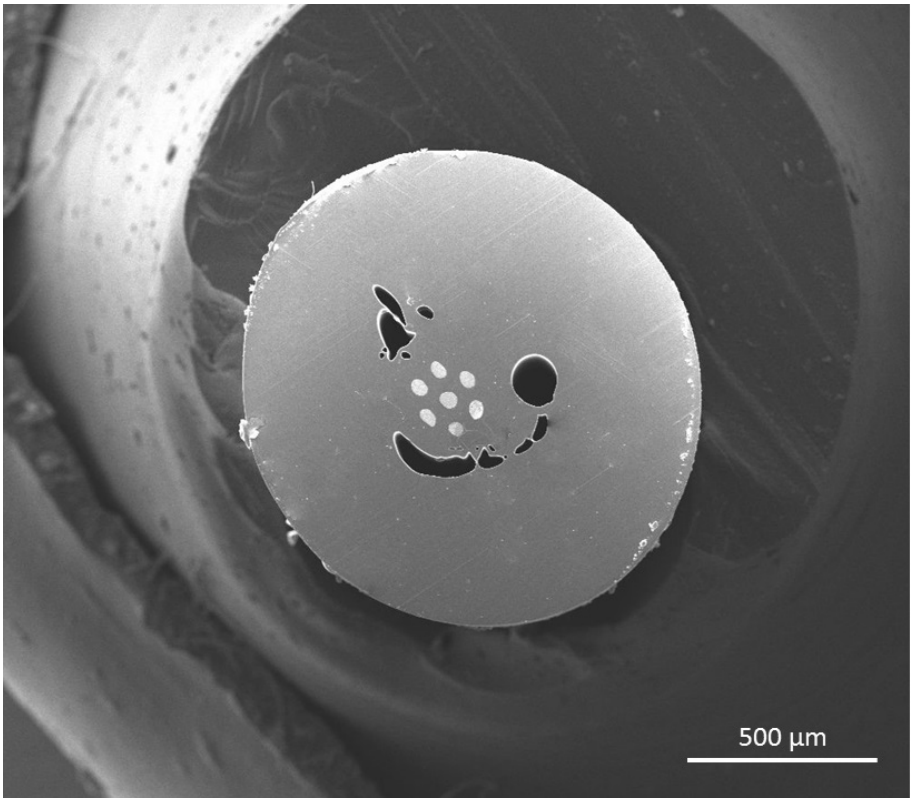

Figure 5.11: The micrograph of the second step fiber. The seven-core design described in Section 3.2 becomes apparent after second step drawing.

Figure 5.12: The preform was prepared for the third step fiber drawing. The second step fibers with seven-core structure were placed to another polymer tube to draw the third step fiber and to obtain the desired diameter.

1.35 μm. The SEM cross sectional image is seen in Figure 5.13, there are compact 34 pieces of seven-core-structured As_2Se_3 core $Ge_{10}As_{23}Se_{67}$ cladding fiber inside a PEI polymer matrix. Figure 5.14 and Figure 5.15 show the structures inside the rectangles on Figure 5.13 named as A and B consecutively. The ChGs fiber preserved their circular shape throughout the drawing processes. The resultant fibers have diameter of around 1.35 μm. The theoretical results at Chapter 3 are calculated based on the resultant fiber diameter after this third step fiber drawing.

In one third step drawing process, it is possible to get all core diameters just by changing drawing parameters while drawing occurs. The ZDW can be engineered to different wavelength for different diameters of core of the fiber. In this way there is no need to draw a new fiber if we need in different scale. Also for high power application polymers may be damaged while pumping. The polymer used can be etched by using dichloromethane (DCM) and get a bundle of all-chalcogenide core-shell fibers then this fiber can be pumped after getting rid of the polymer jacket.

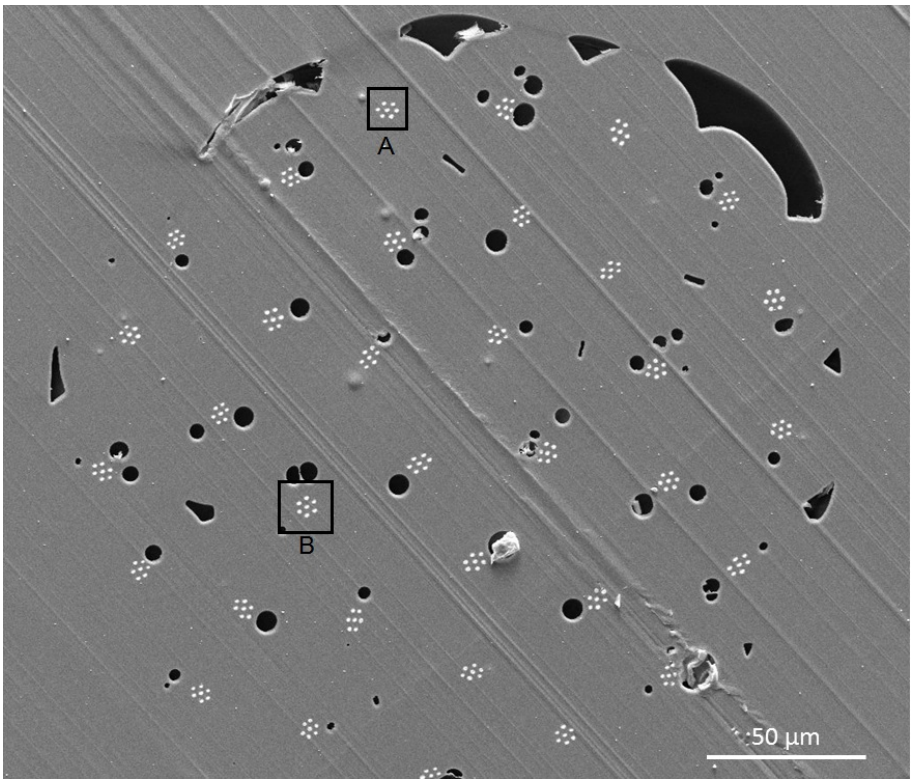

Figure 5.13: Micrograph of the third step fiber. There are 34 seven-core-structure in one fiber. Any of them can be used to obtain SC generation with high output power.

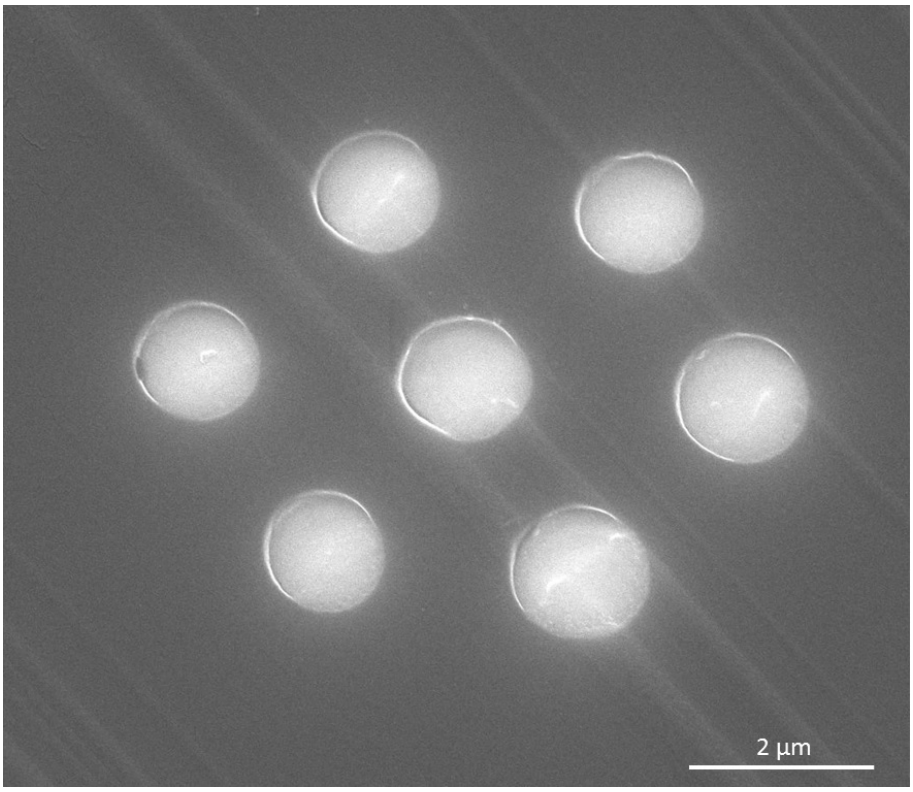

Figure 5.14: The seven-core-structure shown in the rectangle named as A in Figure 5.13

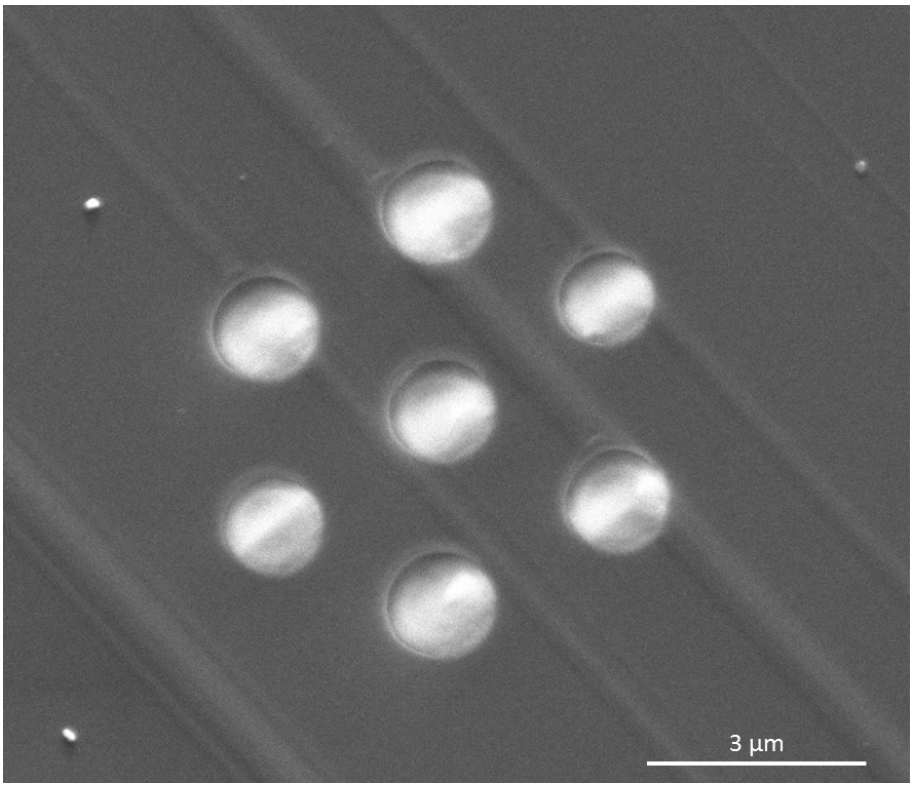

Figure 5.15: The seven-core-structure shown in the rectangle named as B in Figure 5.13

Chapter 6

Conclusion and Future Works

Multicore PCFs are promising for high power SC generation. In literature, we can find very promising results by using seven-core PCF for high power SC generation. The record known for picosecond pulse pumping is 112 W [34]. However, the SC generated covers the range of 0.5-1.7 μm. The SC generation in fingerprint region is possible by using chalcogenide glasses. The SC spans entire fingerprint region has been obtained by using fiber with As_2Se_3 core [3].

In this thesis, we propose a new method to fabricate multicore chalcogenide glasses for the use of high power SC generation. In here, we desired to integrate the merit of multicore structure in high power SC generation and the potential of chalcogenide glasses to generate SC generation in IR region. We designed and fabricated a new seven-core-structured fiber with chalcogenide core/chalcogenide cladding step-index fiber embedded in polyetherimide (PEI) polymer matrix. The ISR method is used to fabricate uniform and size controlled seven-core As_2Se_3 core/$Ge_{10}As_{23}Se_{67}$ cladding optical fibers embedded in polymer (PEI). The preform is produced by using the rod-in-tube approach in three parts as core rod, cladding tube, and the polymer jacket. Melt-quenching in quartz tube is used to fabricate the rod, the rotational casting method is used to fabricate the cladding tube, and for the polymer jacket we used the thin-film rolling followed by consolidation. First of all, the preform is drawn by the help of fiber drawing tower, the

first step fiber is obtained. The fibers obtained after first step drawing are used in second step and they stack in another PEI jacket in such a way that they can preserve the seven-core structure. In the third step drawing we stack 34 pieces of fiber to another PEI jacket and draw it.

We fabricated 34 pieces of the seven-core-structured fiber embedded in one fiber successfully in three successful iterative steps. The pump wavelength is considered as the telecommunication wavelength, 1.55 μm, which is calculated as the ZDW of the fiber which have 0.85 μm As_2Se_3 core diameter (this means the total diameter of chalcogenide is 1.2 μm). We fabricated our ChGs fiber to have the total diameter of 1.35 μm. The theoretical results are calculated based on the resultant fiber diameter after the third step fiber drawing. The corresponding diameter of the core is 0.95 and the dispersion parameter is -100 ps/nm-km which means the GVD is -0.128 ps^2 /m. This value of GVD is very small when we compare it with the bulk material and valid for SC generation.

The refractive indices of these two materials at 1550 nm are 2.73 and 2.61; as a result the NA is engineered to 0.8 at this wavelength. This method allows us to control the NA of the fiber by choosing different materials which are suitable for thermal drawing. The step index structure of the fiber provides the very well confinement of light to the core of the fibers. This enables the more interaction of light with the highly nonlinear part of the fiber and preserves light to be absorbed by the polymer jacket which has high absorbance at IR region. The SSFM calculations show us the broadening of SC is possible from 1 μm to beyond 3.5 μm by using our fiber design.

As future work, the SC measurements needs to be conducted by using high power laser at 1.55 μm. Different pump wavelength can be used for our design with different ChGs diameters. For instance, the capacity of covering entire fingerprint region which is from 1.4 μm to 13.3 μm is proved by the laser light at 6.3 μm pump wavelength coupled to As_2Se_3 core with diameter of 16 μm core which has ZDW of 5.6 μm [3]. With the method we proposed here controlling the diameter of the fiber is easy; therefore we can also fabricate the seven core materials to obtain the entire fingerprint region with high output power.

Bibliography

[1] L. Hooper, *Photonic Crystal Fibres for Coherent Supercontinuum Generation*. PhD thesis, University of Bath, 2012.

[2] J. S. Sanghera, L. B. Shaw, and I. D. Aggarwal, "Applications of chalcogenide glass optical fibers," *Comptes Rendus Chimie*, vol. 5, no. 12, pp. 873–883, 2002.

[3] C. R. Petersen, U. Møller, I. Kubat, B. Zhou, S. Dupont, J. Ramsay, T. Benson, S. Sujecki, N. Abdel-Moneim, Z. Tang, *et al.*, "Mid-infrared supercontinuum covering the 1.4–13.3 μm molecular fingerprint region using ultra-high na chalcogenide step-index fibre," *Nature Photonics*, vol. 8, no. 11, pp. 830–834, 2014.

[4] H. Wei, H. Chen, S. Chen, P. Yan, T. Liu, L. Guo, Y. Lei, J. Li, X. Zhang, J. Hou, *et al.*, "A compact seven-core photonic crystal fiber supercontinuum source with 42.3 w output power," *Laser Phys. Lett*, vol. 10, no. 4, p. 045101, 2013.

[5] G. Tao, H. Ebendorff-Heidepriem, A. M. Stolyarov, S. Danto, J. V. Badding, Y. Fink, J. Ballato, and A. F. Abouraddy, "Infrared fibers," *Adv. Opt. Photon*, 2014.

[6] S. A. Diddams, D. J. Jones, J. Ye, S. T. Cundiff, J. L. Hall, J. K. Ranka, R. S. Windeler, R. Holzwarth, T. Udem, and T. Hänsch, "Direct link between microwave and optical frequencies with a 300 thz femtosecond laser comb," *Physical Review Letters*, vol. 84, no. 22, p. 5102, 2000.

[7] D. J. Jones, S. A. Diddams, J. K. Ranka, A. Stentz, R. S. Windeler, J. L. Hall, and S. T. Cundiff, "Carrier-envelope phase control of femtosecond mode-locked lasers and direct optical frequency synthesis," *Science*, vol. 288, no. 5466, pp. 635–639, 2000.

[8] M. Bellini and T. W. Hänsch, "Phase-locked white-light continuum pulses: toward a universal optical frequency-comb synthesizer," *Optics letters*, vol. 25, no. 14, pp. 1049–1051, 2000.

[9] R. Holzwarth, T. Udem, T. W. Hänsch, J. Knight, W. Wadsworth, and P. S. J. Russell, "Optical frequency synthesizer for precision spectroscopy," *Physical Review Letters*, vol. 85, no. 11, p. 2264, 2000.

[10] G. He, T.-C. Lin, P. Prasad, R. Kannan, R. Vaia, and L.-S. Tan, "New technique for degenerate two-photon absorption spectral measurements using femtosecond continuum generation," *Optics express*, vol. 10, no. 13, pp. 566–574, 2002.

[11] S. Sanders, "Wavelength-agile fiber laser using group-velocity dispersion of pulsed super-continua and application to broadband absorption spectroscopy," *Applied Physics B*, vol. 75, no. 6-7, pp. 799–802, 2002.

[12] Y. Wang, Y. Zhao, J. Nelson, Z. Chen, and R. S. Windeler, "Ultrahigh-resolution optical coherence tomography by broadband continuum generation from a photonic crystal fiber," *Optics Letters*, vol. 28, no. 3, pp. 182–184, 2003.

[13] D. L. Marks, A. L. Oldenburg, J. J. Reynolds, and S. A. Boppart, "Study of an ultrahigh-numerical-aperture fiber continuum generation source for optical coherence tomography," *Optics letters*, vol. 27, no. 22, pp. 2010–2012, 2002.

[14] R. Alfano and S. Shapiro, "Observation of self-phase modulation and small-scale filaments in crystals and glasses," *Physical Review Letters*, vol. 24, no. 11, p. 592, 1970.

[15] R. Alfano and S. Shapiro, "Emission in the region 4000 to 7000 å via four-photon coupling in glass," *Physical Review Letters*, vol. 24, no. 11, p. 584, 1970.

[16] W. Yu, R. Alfano, C. Sam, and R. Seymour, "Spectral broadening of picosecond 1.06 μ pulse in kbr," *Optics Communications*, vol. 14, no. 3, pp. 344–347, 1975.

[17] P. Corkum, P. Ho, R. Alfano, and J. Manassah, "Generation of infrared supercontinuum covering 3–14 μm in dielectrics and semiconductors," *Optics letters*, vol. 10, no. 12, pp. 624–626, 1985.

[18] W. Werncke, A. Lau, M. Pfeiffer, K. Lenz, H.-J. Weigmann, and C. Thuy, "An anomalous frequency broadening in water," *Optics Communications*, vol. 4, no. 6, pp. 413–415, 1972.

[19] W. L. Smith, P. Liu, and N. Bloembergen, "Superbroadening in h 2 o and d 2 o by self-focused picosecond pulses from a yalg: Nd laser," *Physical Review A*, vol. 15, no. 6, p. 2396, 1977.

[20] P. Corkum, C. Rolland, and T. Srinivasan-Rao, "Supercontinuum generation in gases," *Physical review letters*, vol. 57, no. 18, p. 2268, 1986.

[21] V. François, F. Ilkov, and S. Chin, "Experimental study of the supercontinuum spectral width evolution in co 2 gas," *Optics communications*, vol. 99, no. 3, pp. 241–246, 1993.

[22] J. M. Dudley, G. Genty, and S. Coen, "Supercontinuum generation in photonic crystal fiber," *Reviews of modern physics*, vol. 78, no. 4, p. 1135, 2006.

[23] J. K. Ranka, R. S. Windeler, and A. J. Stentz, "Optical properties of high-delta air silica microstructure optical fibers," *Optics letters*, vol. 25, no. 11, pp. 796–798, 2000.

[24] J. K. Ranka, R. S. Windeler, and A. J. Stentz, "Visible continuum generation in air-silica microstructure optical fibers with anomalous dispersion at 800 nm," *Optics letters*, vol. 25, no. 1, pp. 25–27, 2000.

[25] S. Leon-Saval, T. Birks, W. Wadsworth, P. St J Russell, and M. Mason, "Supercontinuum generation in submicron fibre waveguides," *Optics Express*, vol. 12, no. 13, pp. 2864–2869, 2004.

[26] T. Birks, W. Wadsworth, and P. S. J. Russell, "Supercontinuum generation in tapered fibers," *Optics letters*, vol. 25, no. 19, pp. 1415–1417, 2000.

[27] D.-I. Yeom, E. C. Mägi, M. R. Lamont, M. A. Roelens, L. Fu, and B. J. Eggleton, "Low-threshold supercontinuum generation in highly nonlinear chalcogenide nanowires," *Optics letters*, vol. 33, no. 7, pp. 660–662, 2008.

[28] S. Shabahang, M. P. Marquez, G. Tao, M. U. Piracha, D. Nguyen, P. J. Delfyett, and A. F. Abouraddy, "Octave-spanning infrared supercontinuum generation in robust chalcogenide nanotapers using picosecond pulses," *Optics letters*, vol. 37, no. 22, pp. 4639–4641, 2012.

[29] W. Gao, M. Liao, X. Yan, C. Kito, T. Kohoutek, T. Suzuki, M. El-Amraoui, J.-C. Jules, G. Gadret, F. Désévédavy, *et al.*, "Visible light generation and its influence on supercontinuum in chalcogenide as2s3 microstructured optical fiber," *Applied physics express*, vol. 4, no. 10, p. 102601, 2011.

[30] T. Schreiber, J. Limpert, H. Zellmer, A. Tünnermann, and K. Hansen, "High average power supercontinuum generation in photonic crystal fibers," *Optics Communications*, vol. 228, no. 1, pp. 71–78, 2003.

[31] A. K. Abeeluck, C. Headley, and C. G. Jørgensen, "High-power supercontinuum generation in highly nonlinear, dispersion-shifted fibers by use of a continuous-wave raman fiber laser," *Optics letters*, vol. 29, no. 18, pp. 2163–2165, 2004.

[32] K. K. Chen, S.-u. Alam, J. H. Price, J. R. Hayes, D. Lin, A. Malinowski, C. Codemard, D. Ghosh, M. Pal, S. K. Bhadra, *et al.*, "Picosecond fiber mopa pumped supercontinuum source with 39 w output power," *Optics express*, vol. 18, no. 6, pp. 5426–5432, 2010.

[33] X.-h. Fang, M.-l. Hu, L.-l. Huang, L. Chai, N.-l. Dai, J.-y. Li, A. Y. Tashchilina, A. M. Zheltikov, and C.-y. Wang, "Multiwatt octave-spanning

supercontinuum generation in multicore photonic-crystal fiber," *Optics letters*, vol. 37, no. 12, pp. 2292–2294, 2012.

[34] H. Chen, H. Wei, T. Liu, X. Zhou, P. Yan, Z. Chen, S. Chen, J. Li, J. Hou, and Q. Lu, "All-fiber-integrated high-power supercontinuum sources based on multi-core photonic crystal fibers," *Selected Topics in Quantum Electronics, IEEE Journal of*, vol. 20, no. 5, pp. 64–71, 2014.

[35] A. Zakery and S. R. Elliott, *Optical nonlinearities in chalcogenide glasses and their applications*, vol. 135. Springer, 2007.

[36] D. Akbulut, "Lasing action and supercontinuum generation in nano- and micro-structures," Master's thesis, Bilkent University, 2009.

[37] G. P. Agrawal, *Nonlinear fiber optics*. Academic press, 2007.

[38] A. Weiner, *Ultrafast optics*, vol. 72. John Wiley & Sons, 2011.

[39] J.-K. Kim, *Investigation of high-nonlinearity glass fibers for potential applications in ultrafast nonlinear fiber devices*. PhD thesis, Virginia Tech, 2005.

[40] J. C. Knight, "Photonic crystal fibres," *Nature*, vol. 424, no. 6950, pp. 847–851, 2003.

[41] P. Diament, *Wave transmission and fiber optics*. Macmillan publishing company, 1990.

[42] K. J. Blow and D. Wood, "Theoretical description of transient stimulated raman scattering in optical fibers," *Quantum Electronics, IEEE Journal of*, vol. 25, no. 12, pp. 2665–2673, 1989.

[43] N. Yajima and A. Outi, "A new example of stable solitary waves," *Progress of Theoretical Physics*, vol. 45, no. 6, pp. 1997–1998, 1971.

[44] M. Ablowitz and J. Ladik, "Nonlinear difference scheme and inverse scattering," *Studies in Applied Mathematics*, vol. 55, no. 3, pp. 213–229, 1976.

[45] I. t. Greig and J. L. Morris, "A hopscotch method for the korteweg-de-vries equation," *Journal of Computational Physics*, vol. 20, no. 1, pp. 64–80, 1976.

[46] A. Shagalov, "Symplectic integrators for wave equations," *Int. J. Mod. Phys. C*, vol. 10, p. 1, 1999.

[47] J. Ramos, "Linearly implicit methods for the nonlinear schrödinger equation in nonhomogeneous media," *Applied mathematics and computation*, vol. 133, no. 1, pp. 1–28, 2002.

[48] W.-T. Ang and K.-C. Ang, "A dual-reciprocity boundary element solution of a generalized nonlinear schrödinger equation," *Numerical Methods for Partial Differential Equations*, vol. 20, no. 6, pp. 843–854, 2004.

[49] G. Muslu and H. Erbay, "Higher-order split-step fourier schemes for the generalized nonlinear schrödinger equation," *Mathematics and Computers in Simulation*, vol. 67, no. 6, pp. 581–595, 2005.

[50] T. Kremp and W. Freude, "Fast split-step wavelet collocation method for wdm system parameter optimization," *Journal of lightwave technology*, vol. 23, no. 3, p. 1491, 2005.

[51] T. R. Taha and M. J. Ablowitz, "Analytical and numerical aspects of certain nonlinear evolution equations. i. analytical," *Journal of Computational Physics*, vol. 55, no. 2, pp. 192–202, 1984.

[52] K. S. Yee *et al.*, "Numerical solution of initial boundary value problems involving maxwell's equations in isotropic media," *IEEE Trans. Antennas Propag*, vol. 14, no. 3, pp. 302–307, 1966.

[53] J. A. Fleck Jr, J. Morris, and M. D. Feit, "Time-dependent propagation of high energy laser beams through the atmosphere," *Applied Physics*, vol. 10, no. 2, pp. 129–160, 1976.

[54] R. Stolen and A. Ashkin, "Optical kerr effect in glass waveguide," *Applied Physics Letters*, vol. 22, no. 6, pp. 294–296, 1973.

[55] G. Steinmeyer, "Brewster-angled chirped mirrors for high-fidelity dispersion compensation and bandwidths exceeding one optical octave," *Optics express*, vol. 11, no. 19, pp. 2385–2396, 2003.

[56] R. Carman, R. Chiao, and P. Kelley, "Observation of degenerate stimulated four-photon interaction and four-wave parametric amplification," *Physical Review Letters*, vol. 17, no. 26, p. 1281, 1966.

[57] R. Stolen, J. Bjorkholm, and A. Ashkin, "Phase-matched three-wave mixing in silica fiber optical waveguides," *Applied Physics Letters*, vol. 24, no. 7, pp. 308–310, 1974.

[58] C. Lin and R. Stolen, "New nanosecond continuum for excited-state spectroscopy," *Applied Physics Letters*, vol. 28, no. 4, pp. 216–218, 1976.

[59] G. Genty, S. Coen, and J. M. Dudley, "Fiber supercontinuum sources," *JOSA B*, vol. 24, no. 8, pp. 1771–1785, 2007.

[60] J. M. Dudley and J. R. Taylor, *Supercontinuum generation in optical fibers*. Cambridge University Press, 2010.

[61] J. Travers, "Blue extension of optical fibre supercontinuum generation," *Journal of Optics*, vol. 12, no. 11, p. 113001, 2010.

[62] B. J. Eggleton, B. Luther-Davies, and K. Richardson, "Chalcogenide photonics," *Nature photonics*, vol. 5, no. 3, pp. 141–148, 2011.

[63] J. S. Sanghera, L. B. Shaw, and I. D. Aggarwal, "Chalcogenide glass-fiber-based mid-ir sources and applications," *Selected Topics in Quantum Electronics, IEEE Journal of*, vol. 15, no. 1, pp. 114–119, 2009.

[64] J. Wang, E. Vogel, and E. Snitzer, "Tellurite glass: a new candidate for fiber devices," *Optical materials*, vol. 3, no. 3, pp. 187–203, 1994.

[65] T. Schweizer, B. Samson, R. Moore, D. Hewak, and D. Payne, "Rare-earth doped chalcogenide glass fibre laser," *Electronics Letters*, vol. 33, no. 5, pp. 414–416, 1997.

[66] A. Hilton, *Chalcogenide glasses for infrared optics*. McGraw-Hill, Inc., 2010.

[67] X. Zhang, Y. Guimond, and Y. Bellec, "Production of complex chalcogenide glass optics by molding for thermal imaging," *Journal of Non-Crystalline Solids*, vol. 326, pp. 519–523, 2003.

[68] I. Savelii, J. Jules, G. Gadret, B. Kibler, J. Fatome, M. El-Amraoui, N. Manikandan, X. Zheng, F. Désévédavy, J. Dudley, *et al.*, "Suspended core tellurite glass optical fibers for infrared supercontinuum generation," *Optical Materials*, vol. 33, no. 11, pp. 1661–1666, 2011.

[69] R. Stepien, R. Buczynski, D. Pysz, I. Kujawa, A. Filipkowski, M. Mirkowska, and R. Diduszko, "Development of thermally stable tellurite glasses designed for fabrication of microstructured optical fibers," *Journal of Non-Crystalline Solids*, vol. 357, no. 3, pp. 873–883, 2011.

[70] M. Yaman, T. Khudiyev, E. Ozgur, M. Kanik, O. Aktas, E. O. Ozgur, H. Deniz, E. Korkut, and M. Bayindir, "Arrays of indefinitely long uniform nanowires and nanotubes," *Nature materials*, vol. 10, no. 7, pp. 494–501, 2011.

[71] C. C. Wang, "Empirical relation between the linear and the third-order nonlinear optical susceptibilities," *Physical Review B*, vol. 2, no. 6, p. 2045, 1970.

[72] T. Kosa, R. Rangel-Rojo, E. Hajto, P. Ewen, A. Owen, A. Kar, and B. Wherrett, "Nonlinear optical properties of silver-doped as 2 s 3," *Journal of non-crystalline solids*, vol. 164, pp. 1219–1222, 1993.

[73] J. Harbold, F. Ilday, F. Wise, J. Sanghera, V. Nguyen, L. Shaw, and I. Aggarwal, "Highly nonlinear as-s-se glasses for all-optical switching," *Optics Letters*, vol. 27, no. 2, pp. 119–121, 2002.

[74] K. Ogusu, J. Yamasaki, S. Maeda, M. Kitao, and M. Minakata, "Linear and nonlinear optical properties of ag–as–se chalcogenide glasses for all-optical switching," *Optics letters*, vol. 29, no. 3, pp. 265–267, 2004.

[75] M. Liao, C. Chaudhari, G. Qin, X. Yan, T. Suzuki, and Y. Ohishi, "Tellurite microstructure fibers with small hexagonal core for supercontinuum generation," *Optics Express*, vol. 17, no. 14, pp. 12174–12182, 2009.

[76] H. Ebendorff-Heidepriem, P. Petropoulos, S. Asimakis, V. Finazzi, R. Moore, K. Frampton, F. Koizumi, D. Richardson, and T. Monro, "Bismuth glass

holey fibers with high nonlinearity," *Optics Express*, vol. 12, no. 21, pp. 5082–5087, 2004.

[77] T. Kato, Y. Suetsugu, and M. Nishimura, "Estimation of nonlinear refractive index in various silica-based glasses for optical fibers," *Optics letters*, vol. 20, no. 22, pp. 2279–2281, 1995.

[78] Z. Chen, A. J. Taylor, and A. Efimov, "Coherent mid-infrared broadband continuum generation in non-uniform zblan fiber taper," *Optics express*, vol. 17, no. 7, pp. 5852–5860, 2009.

[79] W. Gao, M. El Amraoui, M. Liao, H. Kawashima, Z. Duan, D. Deng, T. Cheng, T. Suzuki, Y. Messaddeq, and Y. Ohishi, "Mid-infrared supercontinuum generation in a suspended-core as 2 s 3 chalcogenide microstructured optical fiber," *Optics express*, vol. 21, no. 8, pp. 9573–9583, 2013.

[80] R. R. Gattass, L. B. Shaw, V. Nguyen, P. Pureza, I. D. Aggarwal, and J. S. Sanghera, "All-fiber chalcogenide-based mid-infrared supercontinuum source," *Optical Fiber Technology*, vol. 18, no. 5, pp. 345–348, 2012.

[81] N. Granzow, S. P. Stark, M. A. Schmidt, A. Tverjanovich, L. Wondraczek, and P. S. J. Russell, "Supercontinuum generation in chalcogenide-silica step-index fibers," *Optics express*, vol. 19, no. 21, pp. 21003–21010, 2011.

[82] J. Hu, C. R. Menyuk, L. B. Shaw, J. S. Sanghera, and I. D. Aggarwal, "Maximizing the bandwidth of supercontinuum generation in as 2 se 3 chalcogenide fibers," *Optics express*, vol. 18, no. 7, pp. 6722–6739, 2010.

[83] P. Domachuk, N. Wolchover, M. Cronin-Golomb, A. Wang, A. K. George, C. Cordeiro, J. C. Knight, and F. Omenetto, "Over 4000 nm bandwidth of mid-ir supercontinuum generation in sub-centimeter segments of highly nonlinear tellurite pcfs," *Optics Express*, vol. 16, no. 10, pp. 7161–7168, 2008.

[84] O. P. Kulkarni, V. V. Alexander, M. Kumar, M. J. Freeman, M. N. Islam, F. L. Terry Jr, M. Neelakandan, A. Chan, *et al.*, "Supercontinuum generation from˜ 1.9 to 4.5 μmin zblan fiber with high average power generation beyond

3.8 μm using a thulium-doped fiber amplifier," *JOSA B*, vol. 28, no. 10, pp. 2486–2498, 2011.

[85] G. Qin, X. Yan, C. Kito, M. Liao, C. Chaudhari, T. Suzuki, and Y. Ohishi, "Ultrabroadband supercontinuum generation from ultraviolet to 6.28 mum in a fluoride fiber," *Applied Physics Letters*, vol. 95, no. 16, p. 1103, 2009.

[86] X. Jiang, N. Y. Joly, M. A. Finger, F. Babic, G. K. Wong, J. C. Travers, and P. S. J. Russell, "Deep-ultraviolet to mid-infrared supercontinuum generated in solid-core zblan photonic crystal fibre," *Nature Photonics*, vol. 9, no. 2, pp. 133–139, 2015.

[87] J. Bei, T. M. Monro, A. Hemming, and H. Ebendorff-Heidepriem, "Fabrication of extruded fluoroindate optical fibers," *Optical Materials Express*, vol. 3, no. 3, pp. 318–328, 2013.

[88] D. Furniss and A. B. Seddon, "Towards monomode proportioned fibreoptic preforms by extrusion," *Journal of non-crystalline solids*, vol. 256, pp. 232–236, 1999.

[89] Y. Ohishi, S. Mitachi, and S. Takahashi, "Fabrication of fluoride glass single-mode fibers," *Lightwave Technology, Journal of*, vol. 2, no. 5, pp. 593–596, 1984.

[90] G. Barton, M. A. van Eijkelenborg, G. Henry, M. C. Large, and J. Zagari, "Fabrication of microstructured polymer optical fibres," *Optical Fiber Technology*, vol. 10, no. 4, pp. 325–335, 2004.

[91] A. Belwalkar, H. Xiao, W. Z. Misiolek, and J. Toulouse, "Extruded tellurite glass optical fiber preforms," *Journal of Materials Processing Technology*, vol. 210, no. 14, pp. 2016–2022, 2010.

[92] D. C. Tran, C. Fisher, and G. Sigel, "Fluoride glass preforms prepared by a rotational casting process," *Electronics Letters*, vol. 18, no. 15, pp. 657–658, 1982.

[93] J. Massera, A. Haldeman, D. Milanese, H. Gebavi, M. Ferraris, P. Foy, W. Hawkins, J. Ballato, R. Stolen, L. Petit, *et al.*, "Processing and characterization of core–clad tellurite glass preforms and fibers fabricated by rotational casting," *Optical Materials*, vol. 32, no. 5, pp. 582–588, 2010.

[94] M. Yamane and Y. Asahara, *Glasses for photonics*. Cambridge University Press, 2000.

[95] V. F. Kokorina, *Glasses for infrared optics*, vol. 13. CRC press, 1996.

[96] J. Orava, J. Šik, T. Wagner, and M. Frumar, "Optical properties of as33s67-xsex bulk glasses studied by spectroscopic ellipsometry," *Journal of Applied Physics*, vol. 103, no. 8, p. 083512, 2008.